

1 **Validating an image-based fNIRS approach with fMRI and a**
2 **working memory task.**

3 Sobanawartiny Wijekumar^a, Theodore Huppert^b, Vincent A. Magnotta^c, Aaron T.
4 Buss^d & John P. Spencer^a

5 a. School of Psychology, University of East Anglia, Norwich, NR4 7TJ

6 b. Department of Radiology, University of Pittsburgh, Pittsburgh PA 15213

7 c. University of Iowa, Department of Radiology and Delta Center, Iowa City

8 52242, Iowa, U.S.A

9 d. University of Tennessee, Department of Psychology, Knoxville, Tennessee

10 37996, U.S.A

11
12 Corresponding authors

13 Sobanawartiny Wijekumar

14 Senior Research Associate

15 School of Psychology

16 University of East Anglia

17 Norwich

18 NR4 7TJ

19 United Kingdom

20 Email: S.Wijekumar@uea.ac.uk

21 Phone number: 0044-07385397211

22
23 John P. Spencer

24 Professor

25 School of Psychology

26 University of East Anglia

27 Norwich

28 NR4 7TJ

29 United Kingdom

30 Email: j.spencer@uea.ac.uk

31

32 **Abstract**

33

34 In the current study, we extend a previous methodological pipeline by adding a
35 novel image reconstruction approach to move functional near-infrared (fNIRS)
36 signals from channel-space on the surface of the head to voxel-space within the
37 brain volume. We validate this methodology by comparing voxel-wise fNIRS
38 results to functional magnetic resonance imaging (fMRI) results from a visual
39 working memory (VWM) task using two approaches. In the first approach,
40 significant voxel-wise correlations were observed between fNIRS and fMRI
41 measures for all experimental conditions across brain regions in the fronto-
42 parieto-temporal cortices. In the second approach, we conducted separate multi-
43 factorial ANOVAs on fNIRS and fMRI measures and then examined the
44 correspondence between main and interaction effects within common regions of
45 interest. Both fMRI and fNIRS showed similar trends in activation within the VWM
46 network when the number of items held in working memory increases. These
47 results validate the image-based fNIRS approach.

48 **Keywords**

49 Functional near-infrared spectroscopy

50 Functional magnetic resonance imaging

51 Visual working memory

52 Image reconstruction

53 Working memory load

54 **Highlights**

- 55 • Novel image reconstruction technique was validated by simultaneously
56 measuring brain activity with fNIRS and fMRI.
- 57 • Both modalities show positive and negative correlations across visual
58 working memory conditions.
- 59 • Both modalities show similar trends in activation in response to increases
60 in working memory load.
- 61

62 **1. Introduction**

63 Functional magnetic resonance imaging is widely considered to be the
64 gold standard for neuroimaging. It provides excellent spatial resolution that has
65 proven useful in a variety of clinical and non-clinical applications. Nevertheless,
66 fMRI has limitations. It does not provide good temporal resolution and there is
67 debate about the origin and nature of the blood oxygen-level dependent signal
68 (BOLD) (Logothetis N.K. Augath M., Trinath T., Oeltermann A, 2001). It is also
69 difficult to use fMRI with infants, children, and some clinical and aging
70 populations because participants need to lie still in the scanner. Finally, fMRI
71 cannot be used to scan people who have 'movable' metal fragments in their
72 body.

73 An alternative neuroimaging technique that overcomes some of these
74 limitations is functional near infrared spectroscopy (fNIRS) (Boas et al., 2014;
75 Ferrari and Quaresima, 2012). fNIRS systems shine near-infrared light at two or
76 more different wavelengths through brain tissue. The two wavelengths of light are
77 differentially absorbed by oxy (HbO) and de-oxy hemoglobin (HbR). Based on
78 this, a localized measure of HbO and HbR concentration in the underlying brain
79 tissue can be determined. Thus, fNIRS provides independent measurements of
80 both chromophores; this has the potential to reveal new insights into
81 neurovascular coupling, particularly given the high temporal resolution of fNIRS.
82 fNIRS can be used with neonates, children, and atypical populations because it
83 is relatively more resistant to motion artifacts. Further, the presence of movable
84 metal fragments is not a limitation with fNIRS. For these reasons, fNIRS has
85 become a neuroimaging tool of choice for these populations. The primary
86 limitation of fNIRS is its poorer spatial resolution relative to fMRI. High quality
87 fNIRS signals can only be obtained from approximately the outer centimeter of
88 cortical tissue. Although this prevents recording from deeper parts of the brain,
89 the spatial resolution obtained in the outer brain tissue is better than that
90 provided by EEG.

91 fNIRS has been widely used to investigate visual, auditory, motor and
92 cognitive stimulation both in non-clinical and clinical settings (Boas et al., 2014;

93 Bortfeld et al., 2009, 2007; Brigadoi et al., 2012; Wijekumar et al., 2012a,
94 2012b). The use of fNIRS in these areas has been spurred forward by validation
95 studies using simultaneous fMRI and fNIRS (Cui et al., 2011; Emir et al., 2008;
96 Erdođan et al., 2014; Fabiani et al., 2014; Huppert et al., 2006, 2005; Maggioni et
97 al., 2015; Muthalib et al., 2013; Okamoto et al., 2004; Pflieger and Barbour,
98 2012; Sakatani et al., 2013; Sassaroli et al., 2005; Sato et al., 2013; Steinbrink et
99 al., 2006; Strangman et al., 2002; Tong and Frederick, 2012; Yücel et al., 2012).
100 These studies have demonstrated good spatial and temporal correlation between
101 both techniques, primarily using tasks that engage the sensorimotor cortices
102 (e.g., finger tapping tasks). Given the increasing number of studies using fNIRS
103 to understand cognition, it is important to validate the use of fNIRS using
104 cognitive tasks to establish whether the correlation between fMRI and fNIRS
105 measures holds beyond the sensorimotor cortex.

106 One cognitive system that has been extensively studied across the
107 lifespan with functional neuroimaging is visual working memory (VWM). VWM is
108 an important cognitive system that accounts for up to 43% of individual
109 differences in global fluid intelligence (Luck and Vogel, 2013). Previous fMRI
110 studies have identified a fronto-parieto-temporal network (Druzgal and
111 D'Esposito, 2003; Learmonth et al., 2001; Linden et al., 2003; Ma et al., 2014;
112 Pessoa and Ungerleider, 2004; Postle, 2015; Rypma et al., 2002; Todd & Marois,
113 R., 2005; Todd and Marois, 2004) that is engaged in VWM tasks as well as parts
114 of this network that are differentially activated by parametric manipulations of, for
115 instance, the working memory load (Todd and Marois, 2004). Most regions in this
116 network fall within the cortical depth measured by fNIRS; thus, VWM is a good
117 target for validating the use of fNIRS in cognitive applications (Cui et al., 2011;
118 Cutini et al., 2011; Fishburn et al., 2014; McKendrick et al., 2014; Molteni et al.,
119 2008; Ogawa et al., 2014; Perlman et al., 2015; Tanaka et al., 2014). To date,
120 two validation studies have correlated fMRI and fNIRS measures in VWM tasks
121 (Cui et al., 2011; Sato et al., 2013). Here, we extend these previous efforts by
122 validating a novel image reconstruction approach to fNIRS data.

123 A central challenge when using fNIRS is that the sensors are placed on
124 the surface of the head, but the questions of interest are about localized activity
125 within the brain volume. Standard fNIRS analysis approaches treat each channel
126 as independent, and significant channel-based effects are often discussed with
127 reference to the 10-20 system of electrode placement. This has several
128 limitations. First, it is difficult to precisely align an fNIRS probe across
129 participants' heads due to variations in head size and shape (Tsuzuki and Dan,
130 2014). For instance, many studies place the optical probes within a rigid body
131 that is then affixed to the head at a particular reference point in the 10-20 system.
132 Although this places the probe over the correct cortical region, slight rotations of
133 the rigid body on the head can create variations in which cortical regions are
134 measured across participants. This challenge is exacerbated with infants, young
135 children, and clinical populations who have difficulty sitting still.

136 Second, by treating each fNIRS channel as independent, researchers fail
137 to capitalize on cases where channels record from overlapping regions of cortex.
138 In such cases, weak effects that live at the intersection of channels might not be
139 detected in channel-based analysis. Third, channel-based analyses make it
140 difficult to compare results across studies and to findings from fMRI studies. It
141 would be ideal if we could, for instance, determine whether an effect reported in
142 an fNIRS study was localized in the same region of cortex as a related effect
143 measured with fMRI. Finally, to date, analytic tools developed in the fNIRS
144 literature are often isolated from analytic tools developed in the fMRI literature
145 and vice versa.

146 One potential solution would be to transform channel-based time-domain
147 fNIRS signals into voxel-based fNIRS activation maps, similar to those reported
148 in fMRI studies. Perlman et al. (2015) used an image reconstruction approach to
149 study activation in response to a VWM task in 3- to 7-year-olds that was based
150 on work by Boas, Culver, and colleagues (Fang and Boas, 2009; Perlman et al.,
151 2015). Here, we build on this and related work (Brigadoi et al., 2015) and ask
152 whether this image reconstruction approach identifies similar clusters of task-
153 related activation within the brain volume measured with simultaneous fMRI.

154 In the sections that follow, we describe the image reconstruction
155 approach. The pipeline we developed builds on a set of methodological tools that
156 help with the design of fNIRS probe geometries (Wijeakumar et al., 2015). Here,
157 we extend these tools, adding a novel image reconstruction approach to move
158 fNIRS signals from channel-space to voxel-space. We then attempt to validate
159 this approach by examining the correspondence between fMRI and image-based
160 fNIRS in response to a VWM task that we adapted from work by Todd and
161 Marois (2004). First, we examine correlations between HbO and HbR and BOLD
162 activation maps. In a second validation step, we look at whether parametric
163 effects measured with fMRI were also evident in the image-based fNIRS results.
164 An important neural signature that has emerged from the fMRI VWM literature is
165 the increase and gradual asymptote in neural activation levels as the working
166 memory load is increased. In the current study, we will hone in on exemplar
167 clusters that show an effect of working memory load and demonstrate that both
168 fNIRS and fMRI show similar trends in activation levels.

169

170 **2. Materials and Methods**

171 2.1. Subjects

172 Thirteen (6 Males; M age = 25.7; SD = 4.2) native English-speaking participants
173 completed the fMRI-fNIRS study. All of them were students at the University of
174 Iowa. All participants had normal or corrected-to-normal vision and signed an
175 informed consent form approved by the Ethics Committee at the University of
176 Iowa.

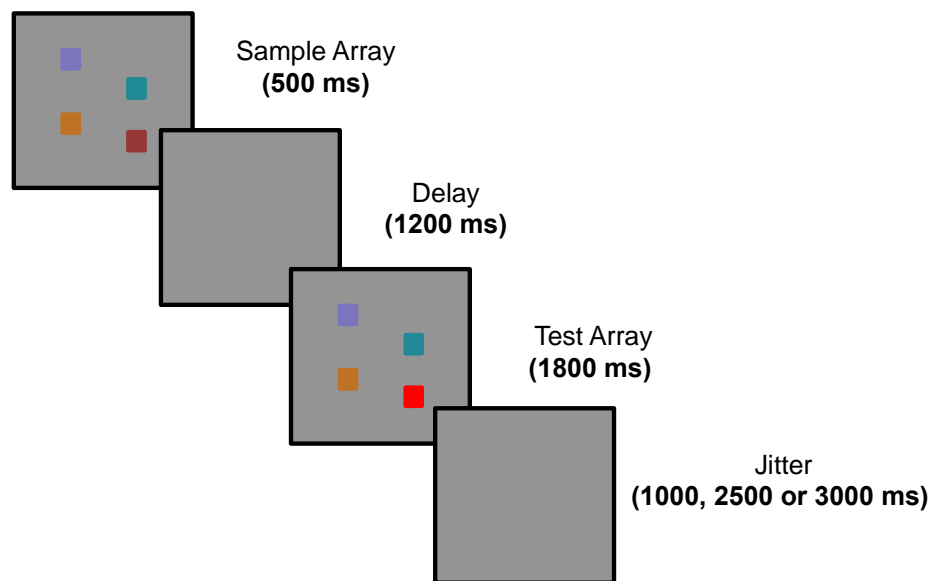
177 2.2. Stimuli and Task Design

178 We used a Change Detection task. The experimental paradigm was created
179 using E-prime version 2.0 and was run on an HP computer (Windows 7).

180 Each trial began with a verbal load of two aurally presented letters; see
181 (Todd and Marois, 2004). At the end of each trial, participants were asked to
182 repeat the presented letters to eliminate the possibility of verbal rehearsal of the
183 colors of the stimuli. Following the presentation of the letters, a Sample array of
184 colored squares (24 x 24 pixels) was presented for 500 ms (randomly sampled

185 from CIE*Lab color-space at least 60° apart). Squares were randomly spaced at
186 least 30° apart along an imaginary circle (100 pixels). The Sample array was
187 followed by a delay of 1200 ms. The delay was followed by the Test array for
188 1800 ms. The Test array was presented with the same number of colored
189 squares as the Sample array, but the Test array could either match the colors of
190 the Sample array ('Same' trials) or the color of a randomly-selected square was
191 shifted 36° in color space ('Different' trials). Participants had to indicate with a
192 button press if the Test array matched the Sample array.

193 Working memory load was manipulated such that two (Load 2), four (Load
194 4) or six (Load 6) squares were presented during the Sample and Test arrays.
195 Participants completed five runs of 120 trials (3 runs at Load 4; 1 run each of
196 Load 2, Load 6) in one of two orders (Load 2, Load 4, Load 6, Load 4, Load 4 or
197 Load 6, Load 4, Load 2, Load 4, Load 4). Three out of thirteen participants did
198 not complete all three runs of Load 4 due to the discomfort of lying in the scanner
199 with the fNIRS sensors attached.



200

201

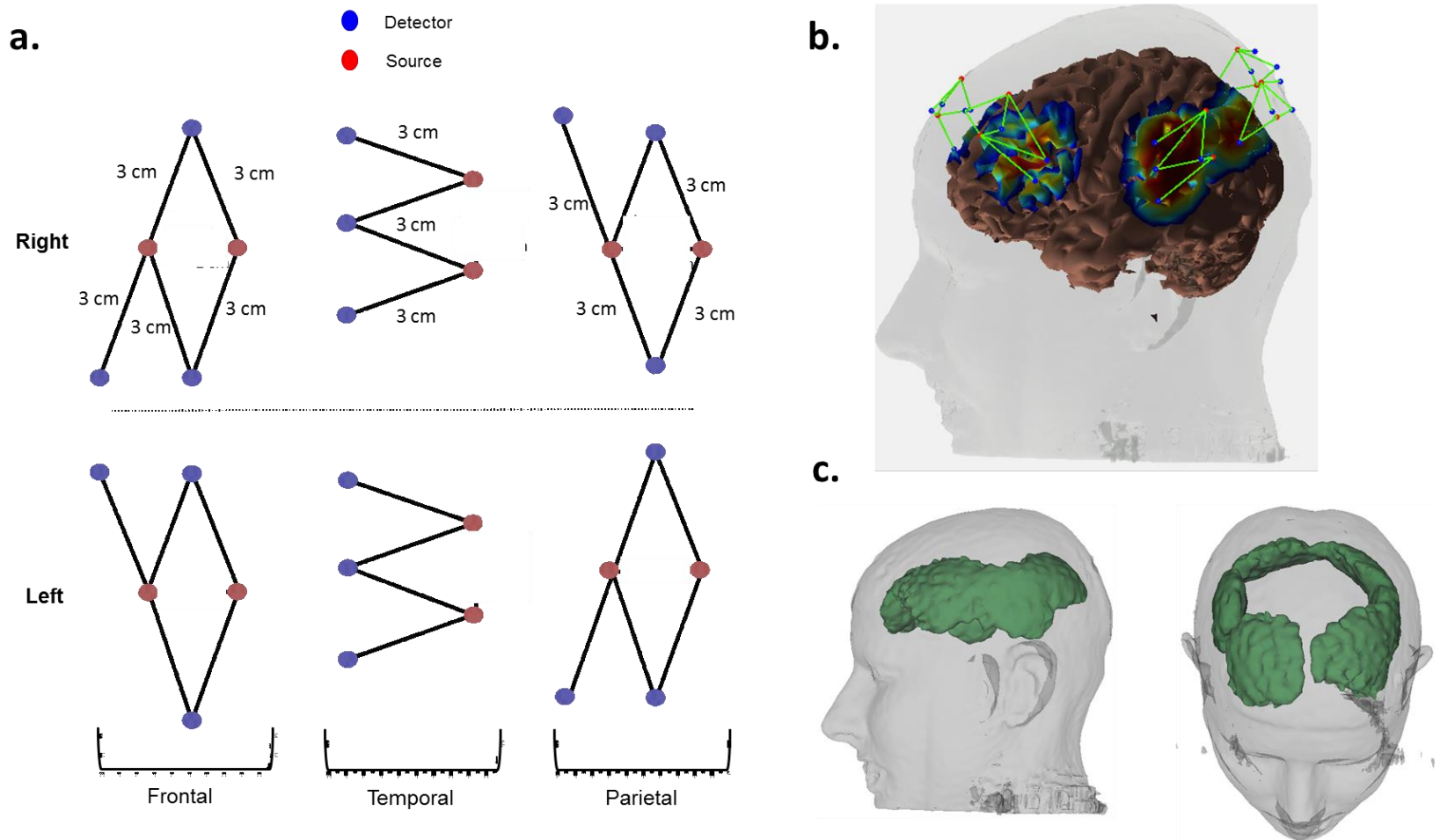
202 Figure 1. Change detection paradigm.

203

204 2.3. fNIRS Acquisition

205 A 24-channel TechEn CW6 (12 sources and 24 detectors) system with
206 wavelengths of 830 nm and 690 nm was used to collect fNIRS data at 25 Hz

207 simultaneously with fMRI data collection. Fiber optic cables were used to deliver
208 light to a customized cap designed for use within the MRI scanner. The cap
209 consisted of channels in 6 arrays covering the left and right frontal, temporal, and
210 parietal regions. Each array consisted of two sources and four detectors. The
211 arrays overlying the frontal and parietal cortices had five channels each with 3
212 cm source-detector (SD) separation and two channels with 1 cm SD separation.
213 The arrays overlying the temporal cortex consisted of four channels with 3 cm SD
214 separation and two channels with 1 cm SD (short source-detector channels)
215 separation. In total, the probe had 40 channels. These arrays were placed on the
216 head relative to the 10–20 system. Note that only six out of the thirteen
217 participants had usable data from the short source-detector channels. Therefore,
218 we did not include data from the short source-detector channels for any of the
219 participants in our analyses. Consequently, we ended up with 28 channels per
220 participant (see Figure 2a). Vitamin E capsules were placed on the fNIRS probe
221 so that the positions of the channels could be detected on the structural scans.
222



223

224 Figure 2 (a) Probe geometry covering the frontal, temporal and parietal cortices. (b) Left hemispheric view of the optodes projected onto a single
 225 subject's head (segmented atlas from MRI scan). Red and blue dots represent sources and detectors and the green lines show respective
 226 channels. (c) 3D representation of the intersected fNIRS-fMRI mask computed across participants.

227 2.4 fNIRS Processing (Steps 1-2 in Figure 3)

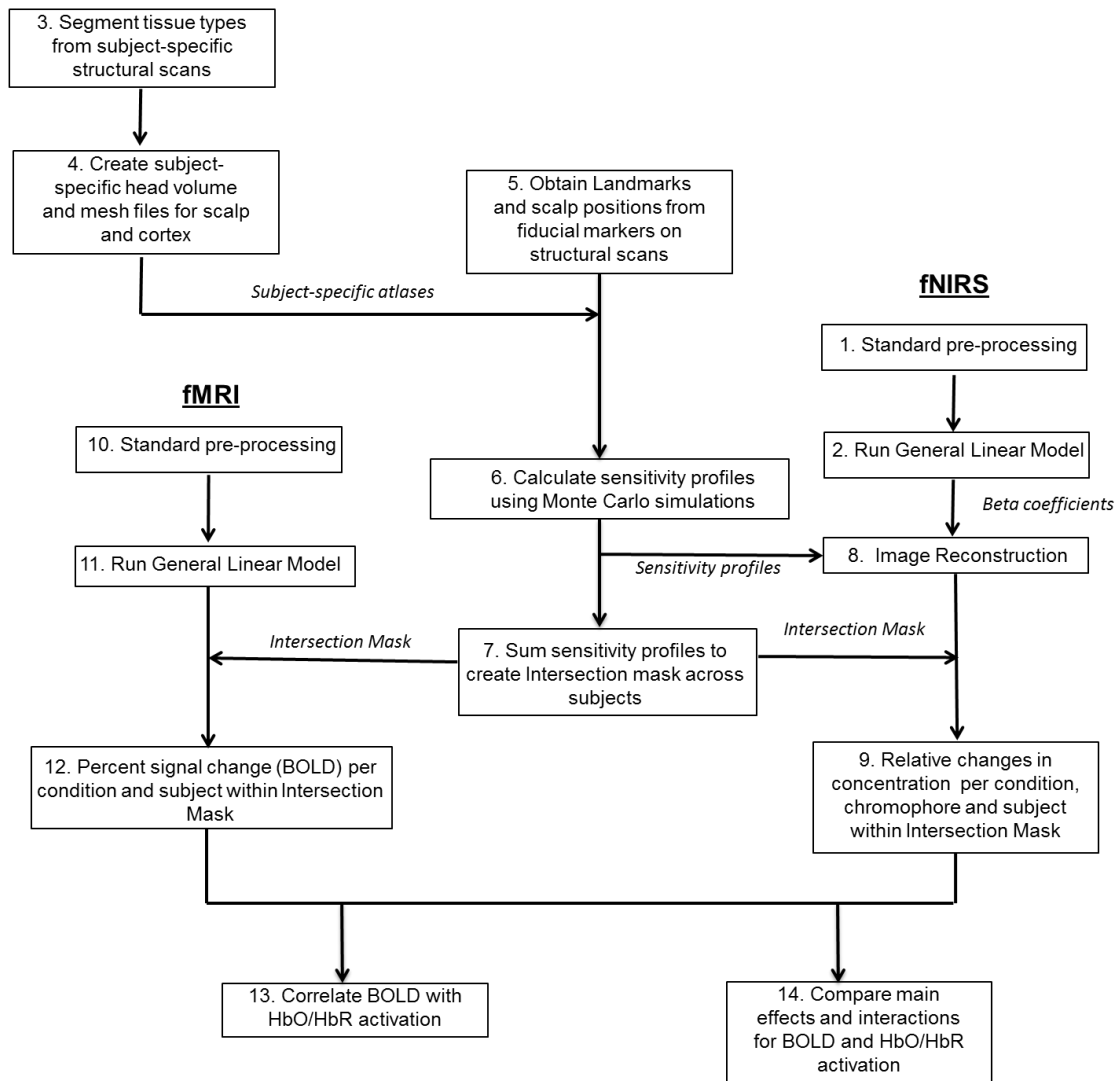
228 Figure 3 shows a flowchart of the processing pipeline. The steps shown in
229 the flowchart are discussed in the following sections.

230 fNIRS data were preprocessed using HOMER2
231 (www.nmr.mgh.harvard.edu/PMI/resources/homer2). Raw data were converted
232 to optical density units. Targeted principal components analysis (AMPTresh =
233 0.5, STDthresh = 50, tMask = 1, and tMotion = 1) was applied to the data to
234 identify and correct motion artifacts (Yücel et al., 2014). The data were then
235 screened for residual motion using motion artifact correction (using the same
236 parameters as above) and those trials that did not meet the criteria were
237 excluded from further analysis. No trials were lost due to motion (there was little
238 motion since participants had to lie still inside the MRI head coil). Data were
239 band-pass filtered (0.016 – 0.5 Hz) to remove low frequency drifts and high
240 frequency noise. Data were then converted to HbO and HbR concentration units
241 using the modified Beer-Lambert Law.

242 Channel-based weighted block averages (used in the majority of previous
243 fNIRS studies) computed across all participants for the Hit condition showed
244 evidence for increasing HbO concentration with increasing working memory load
245 in some channels (see channels 3, 8, 9, 14, 15, 18, 19 and 20 in Supplementary
246 Figure 2). Channel-based weighted block averages for HbR activation have been
247 shown in Supplemental Figure 3. Critically, however, there is limited information
248 about the spatial distribution of these results. Further, in this state, results cannot
249 be directly compared to voxel-based results that fMRI studies yield. To examine
250 these issues, we need to translate these channel-based results to voxel-space
251 using image reconstruction methods. *Note that these conventional channel-*
252 *based block averages are for illustration purposes only; these averages were not*
253 *used below. Rather, the pipeline we developed uses a general linear modeling*
254 *approach that capitalizes on the event-related nature of the experimental design.*

255 To analyze the fNIRS data, a general linear model with 12 regressors was
256 conducted on the HbO and HbR data. The 12 regressors consisted of correct
257 responses on different trials (Hits), correct responses on same trials (CR),

258 incorrect responses on different trials (Miss), and incorrect responses on same
 259 trials (FA) for each of the Load 2, Load 4, and Load 6 runs (4 trial types x 3 loads
 260 = 12 regressors). Regressors were created by convolving the onset of the
 261 Sample array for each of the conditions with a canonical single parameter
 262 gamma variate function. Consequently, we obtained a beta coefficient for each
 263 condition, channel, chromophore, and participant.



264
 265
 266

Figure 3. Flowchart of the processing pipeline

267 Figure 3. Weighted block average HbO signals for Hit trials for Loads 2 (shown in blue), 4 (shown
 268 in green) and 6 (shown in red) across the frontal (outlined in red), temporal (outlined in green) an
 269 and parietal (outlined in blue) channels.

270 2.5. Monte Carlo Simulations (Steps 3-7 in Figure 3)

271 Each participant's structural scan was segmented using *3dSeg* into
272 separate volumes for gray matter, white matter, cerebro-spinal fluid, and scalp
273 tissue. These tissue volumes were identified and assigned unique values. These
274 volumes were then converted to 3D mesh surfaces and merged together to
275 create a subject-specific head atlas using scripts in the *HOMER2* repository
276 (Wijeakumar et al., 2015). We chose to use subject-specific structural scans
277 instead of a generic adult atlas following findings from Cooper and colleagues
278 (Cooper et al., 2012). They reported that the Euclidean error in localization with
279 reference to a center of activation increased two-fold when an atlas was used
280 instead of a segmented atlas from the individual's MRI scan.

281 *Slicer3D* was used to visualize and then extract the scalp landmarks and
282 positions of sources and detectors from Vitamin E capsules placed on the
283 structural scans of the participants. *AtlasViewerGUI* (available within *HOMER2*:
284 www.nmr.mgh.harvard.edu/PMI/resources/Homer2) was then used to project
285 these points onto an each participant's head atlas using a relaxation algorithm. A
286 single subject's projected probe geometry is shown in Figure 2b. The projected
287 geometry was used to run Monte Carlo simulations (with 100 million photons)
288 based upon a GPU-dependent Monte Carlo algorithm (Fang and Boas, 2009).
289 The output of the Monte Carlo simulations yield a sensitivity distribution that is
290 representative of the sensitivity of each channel to detecting changes in the
291 cortical absorption of near infrared light. Thus, we obtained sensitivity profiles for
292 each of the 28 channels for each participant.

293 The sensitivity profiles and the head volumes were converted to nifti
294 images. Subject-specific head volumes were skull-stripped and transformed from
295 the *AtlasViewerGUI* space to the native subject space using an affine transform
296 (*BRAINSFit in Slicer 3D*). This transformation matrix was also applied to the
297 sensitivity profiles to move them back to the native subject space
298 (*BRAINSResample in Slicer3D*). The sensitivity profiles for each participant were
299 summed together to create a subject-specific mask that represented the spatial
300 distribution of cortical volume that fNIRS signals were most likely recorded from.

301 These subject-specific masks were thresholded to include voxels with an optical
302 density of greater than 0.0001, a robust threshold value that is derived from our
303 previous work (Wijeakumar et al., 2015).

304 Next, the head volumes in native subject space were transformed from
305 native subject space to MNI space using an affine transform with nine
306 parameters (using *3dAllineate*). These transformation matrices were further used
307 to transform the subject-specific masks to MNI space. These subject-specific
308 masks were summed together and masked such that only voxels that contained
309 a value greater than 7 were retained. Thus, we created a group intersection
310 mask across participants wherein at least seven out of thirteen participants
311 contributed to a voxel. A decimated and smoothed version of a single
312 participant's head volume and the group intersection mask (created using
313 *ModelMaker in Slicer 3D*) is shown in Figure 2c.

314

315 2.6. Image Reconstruction (Step 8-9 in Figure 3)

316 The majority of fNIRS studies have utilized channel-based time-domain
317 analyses. Although informative, such approaches provide only limited information
318 about localization, typically with reference to the 10-20 positions of channels on
319 the head. This can be problematic, because the positions of sources and
320 detectors invariably differ across participants, particularly when working with
321 special populations such as infants, young children, or clinical populations who
322 have difficulty sitting still. Moreover, channel-based analyses fail to capitalize on
323 the fact that nearby fNIRS channels often record overlapping signals; such
324 information is lost by treating each channel as independent. Finally, the absence
325 of good localization tools in fNIRS research limits comparisons with the large
326 body of fMRI research. Hence, the goal of our study was to validate a new image
327 reconstruction approach in a cognitive task.

328 To generate functional images from the fNIRS data, the beta coefficients
329 obtained for each condition, channel, and participant (see section 2.4) must be
330 combined with the sensitivity profiles obtained from the Monte Carlo simulations
331 (see section 2.5) to create voxel-based changes in HbO and HbR concentration.

332 The relationship between the hemodynamic response (estimated by the beta
 333 coefficients from the GLM) in HbO/HbR concentration and that in delta-optical
 334 density is given by:

$$335 \quad \beta_{dOD}^\lambda = ppf^\lambda \cdot d \cdot \varepsilon_{HbO}^\lambda \cdot \beta_{HbO} + ppf^\lambda \cdot d \cdot \varepsilon_{HbR}^\lambda \cdot \beta_{HbR} \quad (1)$$

336 where, d is the source-detector distance, ε is the extinction coefficient for
 337 each wavelength (λ) and ppf is the partial pathlength factor (Li et al., 2004).

338 Equation (1) can be re-written to accommodate the forward model and
 339 betas from each channel for each wavelength to estimate voxel-wise changes in
 340 HbO and HbR concentrations,

$$341 \quad \begin{bmatrix} d \cdot \varepsilon_{HbO}^{\lambda_1} \cdot \beta_{HbO} + d \cdot \varepsilon_{HbR}^{\lambda_1} \cdot \beta_{HbR} \\ d \cdot \varepsilon_{HbO}^{\lambda_2} \cdot \beta_{HbO} + d \cdot \varepsilon_{HbR}^{\lambda_2} \cdot \beta_{HbR} \end{bmatrix} = \begin{bmatrix} \varepsilon_{HbO}^{\lambda_1} \cdot F^{\lambda_1} & \varepsilon_{HbR}^{\lambda_1} \cdot F^{\lambda_1} \\ \varepsilon_{HbO}^{\lambda_2} \cdot F^{\lambda_2} & \varepsilon_{HbR}^{\lambda_2} \cdot F^{\lambda_2} \end{bmatrix} \cdot \begin{bmatrix} \Delta HbO_{vox} \\ \Delta HbR_{vox} \end{bmatrix} \quad (2)$$

342 where, F is the channel-wise sensitivity volumes from the Monte Carlo
 343 simulations. ΔHbO_{vox} and ΔHbR_{vox} are voxel-wise relative changes in HbO and
 344 HbR concentrations – this is what we want to estimate in the image
 345 reconstruction process. *Note that β and F are obtained for each channel and are*
 346 *represented as arrays within the matrix above.*

347 We can re-write equation Equation (2) as,

$$348 \quad Y = L \cdot X \quad (3)$$

349 where,

$$350 \quad Y = \begin{bmatrix} \beta_{dOD}^{\lambda_1} \\ \beta_{dOD}^{\lambda_2} \end{bmatrix}$$

$$351 \quad L = \begin{bmatrix} \varepsilon_{HbO}^{\lambda_1} \cdot F^{\lambda_1} & \varepsilon_{HbR}^{\lambda_1} \cdot F^{\lambda_1} \\ \varepsilon_{HbO}^{\lambda_2} \cdot F^{\lambda_2} & \varepsilon_{HbR}^{\lambda_2} \cdot F^{\lambda_2} \end{bmatrix}$$

$$352 \quad X = \begin{bmatrix} \Delta HbO_{vox} \\ \Delta HbR_{vox} \end{bmatrix}$$

353

354 Inverting L to solve for X results in an ill-conditioned and under-determined
 355 solution that might be subject to rounding errors. An alternative is to use a
 356 popular regularization method called Tikhonov regularization (Tikhonov A.,
 357 1963). In this case, the above ‘system’ can be replaced by a regularized ‘system’.
 358 The solution is given by the Gauss-Markov equation,

$$359 \quad X = (L^T L + \lambda \cdot I)^{-1} L^T \cdot Y \quad (4)$$

360 where λ is a regularization parameter that determines the amount of
361 regularization and I is the identity operator.

362 The solution to (4) can be found by minimizing the cost function (Calvetti
363 et al., 2000),

$$364 \quad \text{cost} \min X = |L \cdot X - Y|^2 + \lambda \cdot |X - X_0|^2 \quad (5)$$

365 where the size of the regularized solution is measured by the norm $\lambda \cdot |X - X_0|^2$.
366 X_0 is a priori estimate of X , which is set to zero when no priori information is
367 available. Picking the appropriate regularization parameter is dependent on the
368 trade-off between fitting Y and maintaining a small residual (if too much
369 regularization is applied) and eliminating the contributions of data and rounding
370 errors (if too little regularization is applied). Hence, an L-curve is plotted between
371 the norms of the solution and the residual. The corner of this L-curve is identified
372 and the corresponding regularization parameter is used to estimate X .

373 Here X is determined for each chromophore and condition (12 conditions)
374 separately. Once we solve (5), we have a voxel-wise estimate of the
375 concentration data. Thus, we have moved from our best estimate of the channel-
376 wise concentration data for each condition (from the GLM) and combined this
377 information with the sensitivity profiles to create an estimate of the voxel-wise
378 relative changes in concentration for each condition, for each subject and, for
379 each chromophore. These maps were transformed to the MNI space by using the
380 transformation matrix (affine transformation with 9 parameters) generated from
381 transforming the subject-specific head volumes. Finally, these voxel-wise relative
382 changes in chromophore concentration were multiplied by the group intersection
383 mask and moved forward to the group analyses.

384

385 2.7. fMRI Acquisition and Processing (Steps 10-12 in Figure 3)

386 fMRI data were collected in a 3T Siemens TIM Trio scanner using a 12-
387 channel head coil. Anatomical T1 weighted volumes were collected using an MP-
388 RAGE sequence. Functional BOLD imaging was acquired using an axial 2D
389 echo-planar gradient echo sequence with the following parameters: TE=30ms,

390 TR=2000ms, flip angle=70°, FOV=240x240mm, matrix=64x64, slice
391 thickness/gap=4.0/1.0mm, and bandwidth=1920Hz/pixel.

392 AFNI was used to perform standard pre-processing such as slice timing
393 correction, outlier removal, motion correction, and spatial smoothing (Gaussian
394 FWHM=5mm). Nuisance regressors of motion correction, baseline drift, and 12
395 standard model regressors (12 conditions – as specified in section 2.4) were
396 used in a general linear model (using *3dDeconvolve*). Polynomials of the third
397 order were used as regressors to account for drift in the data and serve as a high
398 pass filter. *Note that, BOLD data were analyzed using conventional parameters*
399 *from fMRI literature and not with parameters used for the fNIRS analyses.* The
400 onset of the sample array for each condition was convolved with a canonical
401 single parameter gamma variate function. This function was identical to that used
402 in the GLM for the fNIRS data. Betamaps (in percent BOLD signal) were
403 obtained for each model regressor and for each participant. An affine
404 transformation was applied to each individual's skull-stripped T1 scan to
405 transform it to the MNI space. This transformation matrix was used to transform
406 the betamaps to the MNI space. Finally, these betamaps were multiplied by the
407 group intersection mask (see step 8) and moved forward to the group analyses.

408

409 2.7. Statistical Analysis

410 2.7.1 Behavioral Analysis

411 Only correct trials across Load (2, 4 and 6) and Trial type (Same and Different)
412 were analyzed using a two-factorial ANOVA in SPSS 21.

413

414 2.7.2 Correlations between BOLD and NIRS signals within the VWM 415 network (Step 13 in Figure 3)

416 Previous validation studies have reported good spatial and temporal
417 correlations when comparing fNIRS and fMRI signals. In the current study, we
418 wanted to investigate whether the betamaps produced from our image
419 reconstruction methods were spatially correlated with the BOLD betamaps.

420 We carried out Pearson's voxel-wise correlations between the BOLD
421 betamaps and relative changes in HbO and HbR concentration for each of the 12
422 conditions separately. We thresholded each of our correlation maps using a
423 voxel-wise threshold of $p < 0.05$, $\alpha < 0.05$ and a cluster size of 28 voxels (obtained
424 using *3dClustSim*) based on the size of the group intersection mask, size of the
425 3D grid of the image (91 x 109 x 91 voxels), and the voxel size (2mm) of the
426 image. Further, voxels were clustered together only if faces or edges touched.
427 For specific exemplar clusters, average R-values were calculated within each
428 cluster for each participant using *3dROIstats*.

429 To estimate the depth of the voxel with the highest correlation in each
430 cluster, the shortest Euclidean distance between the voxel with the highest
431 correlation and the surface of the brain was calculated.

432

433 2.7.3 Multi-factorial effects common to BOLD and NIRS (Step 14 in
434 Figure 3)

435 Previous research with fMRI has reported key regions in the frontal,
436 parietal, and temporal cortices involved in processing changes in a working
437 memory task. Hence, in the current study, we examined whether the same
438 regions showing an effect in working memory processing, for instance, with fMRI
439 would also show comparable parametric effects with fNIRS.

440 To achieve this, the BOLD betamaps were analyzed at the group level
441 using a three-factor ANOVA with Load (2,4,6), Trial type (Same, Different), and
442 Accuracy (Correct, Incorrect) as within-subjects factors. Similarly, for fNIRS, the
443 betamaps for the relative changes in HbO and HbR concentration were analyzed
444 at the group-level using two separate 3-factor ANOVAs (Load x Trial type x
445 Accuracy), one for each chromophore. The main effects and interactions from all
446 three ANOVAs (BOLD, HbO and HbR) were thresholded to correct for familywise
447 errors (voxel-wise threshold of $p < 0.05$, $\alpha < 0.05$, and a cluster size of 28 voxels).
448 We then identified significant clusters where both fMRI and fNIRS showed the
449 same statistically significant main effect or interaction. Further, the spatial maps

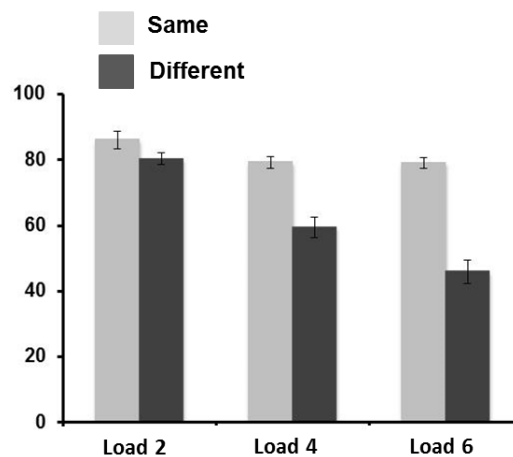
450 for the main effect of Load were compared between BOLD and fNIRS to highlight
451 exemplary effects.

452

453 3. Results

454 3.1. Behavioral results

455 Figure 4 shows the accuracy rates in percentage across Load and Trial
456 types. Briefly, there were main effects of load ($F_{(2,24)}=57.40$, $p<0.001$) and Trial
457 type ($F_{(1,12)}=50.85$, $p<0.001$) and the interaction between Load and Trial type
458 ($F_{(2,24)}=57.40$, $p<0.001$) was also significant. Post-hoc comparisons revealed that
459 same trials had higher accuracy rates than different trials ($p<0.001$). Accuracy
460 rates decreased with an increase in Load ($p<0.05$). Further comparisons of the
461 interaction between Trial type and Load revealed that accuracy significantly
462 decreased as a function of Load only for the different trials ($p<0.005$). Further,
463 only at Load 4 and 6, did same trials have significantly higher accuracy rates
464 than different trials ($p<0.001$).



465

466 Figure 4. Accuracy (%) plotted across same and different trials for Loads 2,4 and 6.

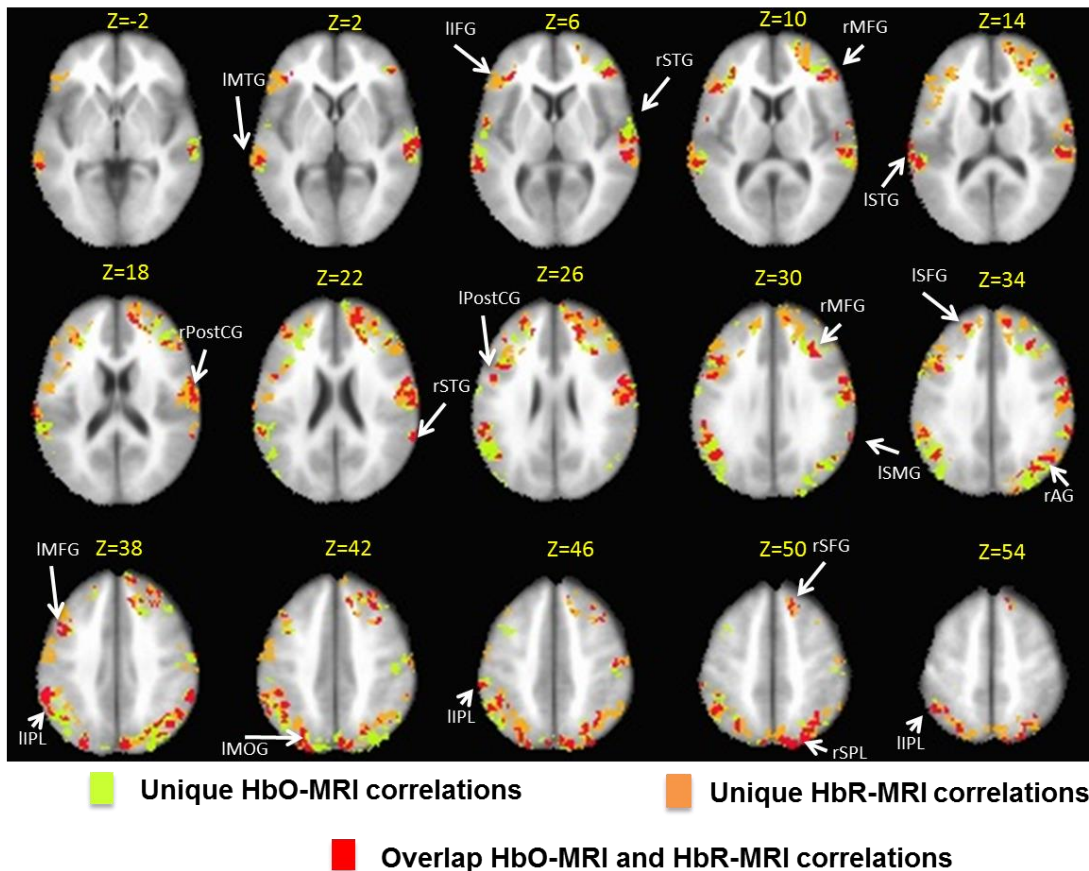
467

468 3.2 Correlations between BOLD and image-reconstructed fNIRS signals

469 Figure 5 shows a montage of the cortical regions where there was a
470 significant correlation between BOLD and HbO/HbR concentration following
471 familywise correction. As can be seen in the figure, the two signals correlated
472 significantly across many areas central to the VWM network, including middle
473 (MFG), inferior (IFG) and superior frontal gyrus (SFG), superior (SPL) and

474 inferior parietal lobule (IPL), superior (STG) and middle temporal gyri (MTG),
 475 precuneus and cuneus. *Note that regions of overlap across HbO-BOLD and*
 476 *HbR-BOLD correlations do not necessarily occur across the same conditions.*

477 When we examined the nature of these correlations in detail, we observed
 478 significant positive and negative correlations between HbO and BOLD and HbR
 479 and BOLD signals. Positive HbO-BOLD and positive HbR-BOLD correlations
 480 accounted for 22.9% and 29.7% of the all the correlations, respectively.
 481 Interestingly, negative HbO-BOLD and negative HbR-BOLD correlations
 482 accounted for 25.6 % and 21.6 % of all the correlations, respectively. *Note that a*
 483 *voxel could show positive correlations between HbO and BOLD for a specific*
 484 *condition and negative correlations for another condition.* A complete breakdown
 485 of the correlation types across conditions is reported in Supplemental table T1.
 486



487
 488 Figure 5. Montage showing correlations between relative changes in HbO/HbR concentration and
 489 percent BOLD signal change. Note that the spatial distributions have been masked to create

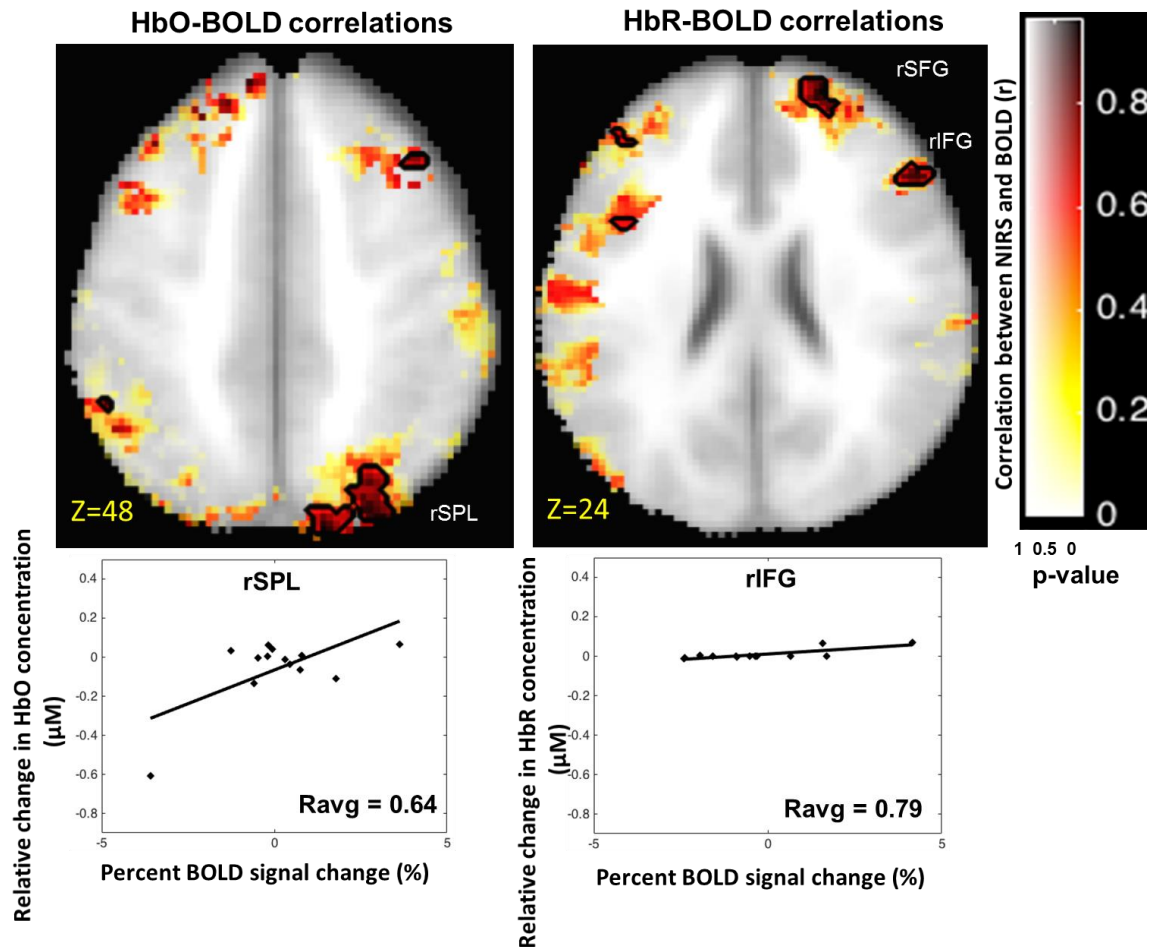
490 binary images. The green color indicates clusters with significant HbO-MRI correlations, but not
491 HbR-MRI correlations; orange indicates clusters with significant HbR-MRI correlations, but not
492 HbO-MRI correlations; red indicates clusters with significant correlations between both
493 chromophores and MRI.

494 When pooled across loads, Hit and CR conditions showed more
495 significant correlations between HbO and fMRI (Hits = 1824 voxels and CR =
496 1243 voxels) than the FA and Miss conditions (see Supplementary Table T1 for
497 details). Further, we were particularly interested in the Load 4 condition as
498 previous research has suggested that the capacity limit for visual working
499 memory is around four items (Luck and Vogel, 1997). Thus, to examine the
500 nature of the correlations in greater detail, we focused on the Hit4 and CR4
501 conditions.

502 Figures 6 and 7 show positive correlations across voxels for HbO-BOLD
503 and HbR-BOLD correlations for the Hit4 and CR4 conditions, respectively. These
504 figures also show scatter plots of correlation values averaged across voxels in
505 clusters that met the family-wise correction threshold (28 voxels). For the Hit4
506 condition, the magnitude of the peak correlation values from each significant
507 cluster for positive HbO-BOLD and positive HbR-BOLD correlations ranged from
508 0.71 to 0.99. For the CR4 condition, the peak correlation values from each
509 significant cluster for positive HbO-BOLD and positive HbR-BOLD correlations
510 ranged from 0.62 to 0.97. As is evident from the figures, there were clusters with
511 significant positive HbO-BOLD correlations in the rSPL for both Hit4 and CR4
512 conditions. Similarly, there were clusters with significant positive HbR-BOLD
513 correlations in the rIFG for both Hit4 and CR4 conditions (for a complete listing of
514 clusters with significant correlations, see supplementary tables T2-T5).

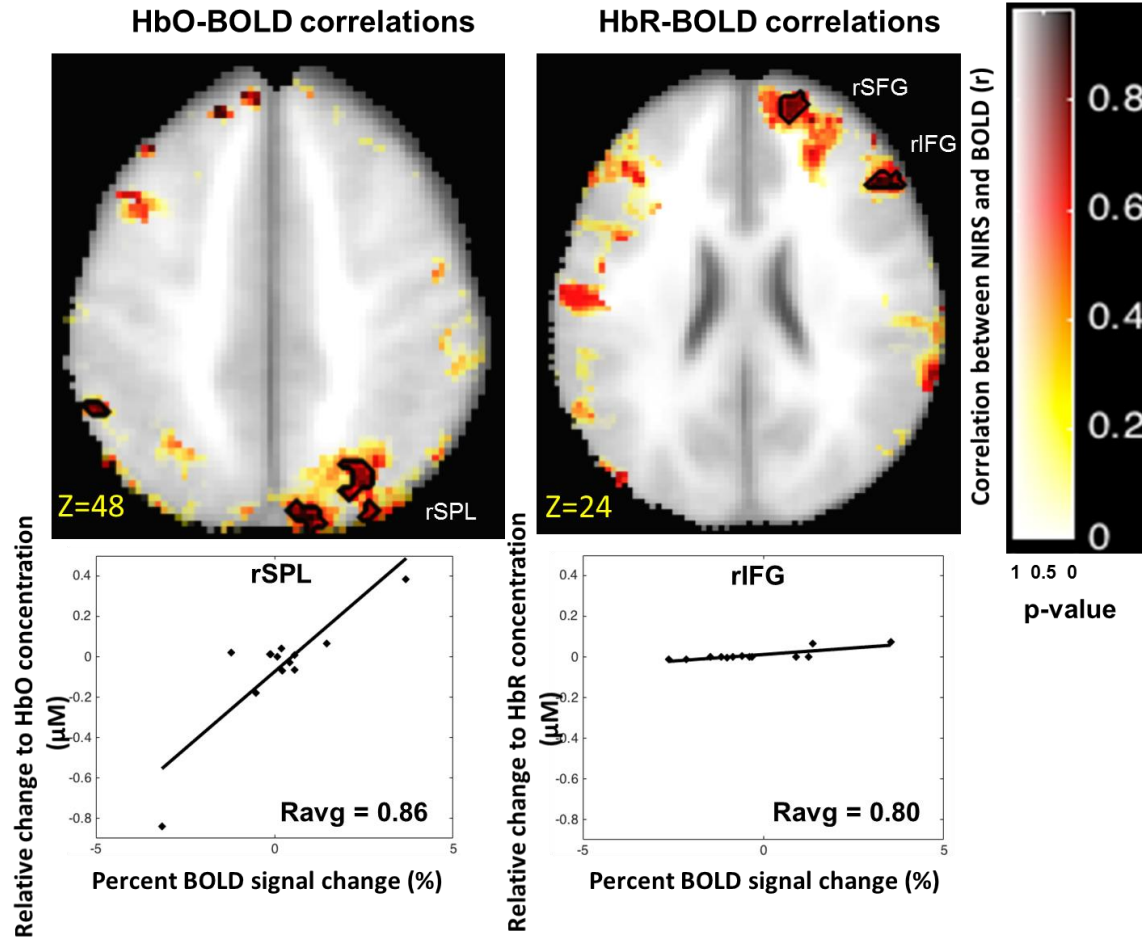
515 Previous studies have reported that the depth of voxels showing
516 correlations between BOLD and fNIRS measures were between 15-20 mm (Cui
517 et al., 2011; Schroeter et al., 2006). Thus, we estimated the depth of the voxels
518 within each cluster with the highest correlations between HbO and BOLD and
519 HbR and BOLD for Hit4 and CR4 conditions. The mean depth (from the surface
520 of the brain) of the most highly correlated voxels between fNIRS and BOLD was
521 5.6 ± 0.8 mm (positive HbO-BOLD correlation depth = 4 mm and positive HbR-

522 BOLD correlation depth = 7.1 mm). Taken together with an average estimation
 523 for scalp and skull thicknesses (11-13 mm), the depth of these correlations from
 524 the surface of the scalp is between 15-20 mm, which is in agreement with these
 525 previous studies (Cui et al., 2011; Schroeter et al., 2006).



526
 527 Figure 6. Positive HbO-BOLD and HbR-BOLD correlations for the Hit4 condition. Clusters that
 528 reached significance ($p < 0.05$) are shown within contours. Transparency of clusters in the image
 529 indicates significance (as represented by the x-axis of the color scale). Scatter plots for selected
 530 clusters are shown below the respective correlation image. Ravg (shown in the correlation plots)
 531 was obtained for each participant ($N=13$) by averaging the r values across all voxels of a
 532 significant cluster.

533
 534
 535



536

537

538

539

540

541

542

Figure 7. Positive HbO-BOLD and HbR-BOLD correlations for the CR4 condition. Clusters that reached significance ($p < 0.05$) are shown within contours. Transparency of clusters in the image indicates significance (as represented by the x-axis of the color scale). Scatter plots for selected clusters have been shown below the respective correlation image. R_{avg} (shown in the correlation plots) represents correlation of data from 13 participants obtained from averaging r values across all voxels of a significant cluster.

543 3.4 Overlapping multi-factorial VWM effects

544 The current validation study is embedded within a cognitive task with
545 parametric manipulations. Do fNIRS and fMRI detect the same changes in
546 activation levels as a function of these parametric manipulations? To evaluate
547 this question, we conducted three 3-factor ANOVAs -- one for BOLD, one for
548 HbO, and one for HbR (see Methods)--and examined the degree to which
549 significant effects overlapped and yielded the same activation patterns across
550 experimental manipulations.

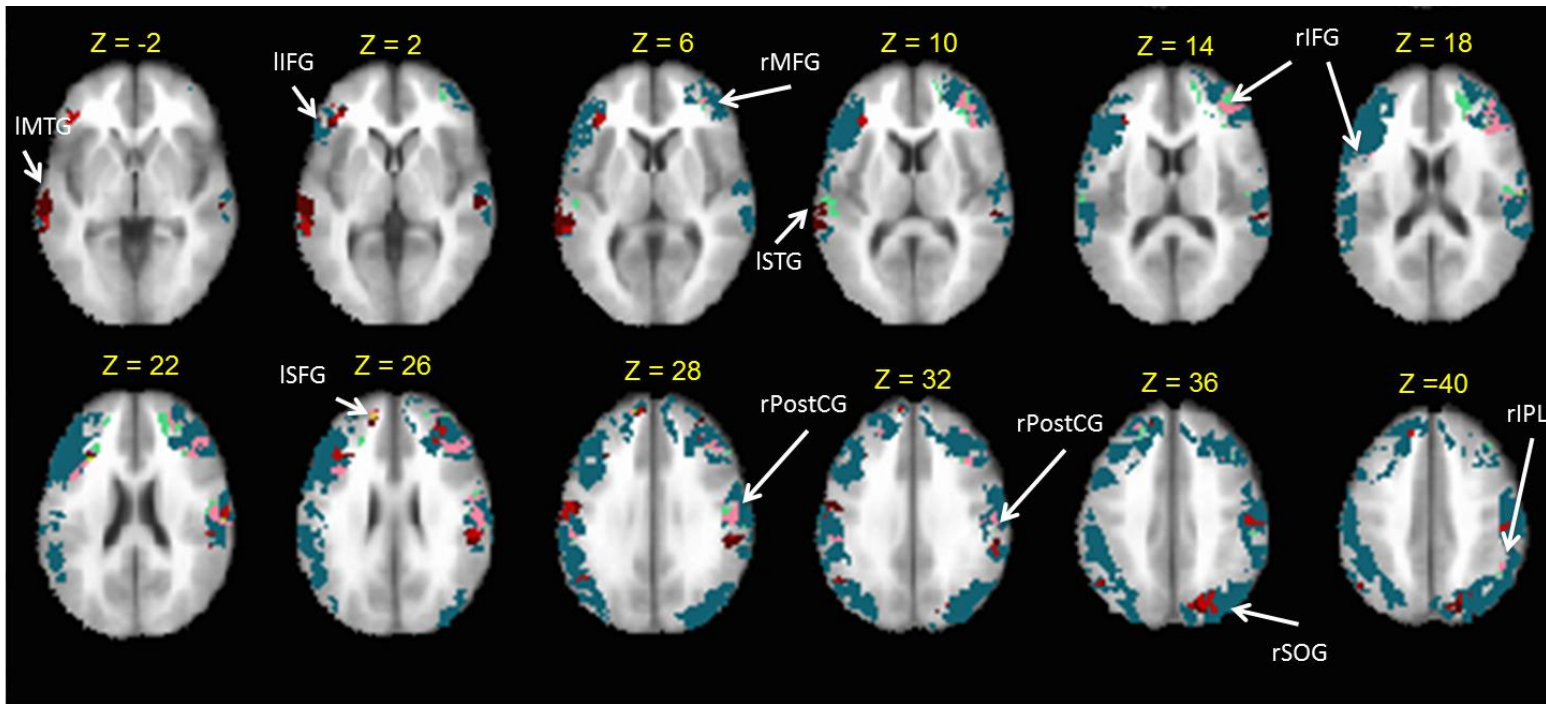
551 Figure 8 shows a montage image of the overlapping and unique effects
552 from the significant ANOVA results following family-wise correction. There is
553 overlap between the fNIRS and BOLD effects across parts of the fronto-parieto-
554 temporal regions such as IPL, MFG, SFG and IFG. Although there is overlap
555 between the modalities, however, the fNIRS effects are much more focal
556 compared to the spatial distribution of the BOLD effects. As we discuss below,
557 this may reflect differences in the signal-to-noise ratio of the two modalities. *Note*
558 *that overlap between HbO, HbR and MRI accounted for only 15 voxels (summed*
559 *across all cortical regions) and this has not been shown in Figure 8.*

560 Within the regions of overlap, a central issue is whether the two modalities
561 are detecting the same parametric effect. Tables 1 and 2 show all clusters that
562 had overlapping main effects and interaction effects for HbO and BOLD and HbR
563 and BOLD ANOVAs, respectively. There was substantial overlap in effects
564 across key parts of the visual working memory network. This included large
565 clusters with overlapping Load main effects in rIPL and rMFG for the comparison
566 between HbO and BOLD. There were also large clusters with overlapping Load x
567 Trial x Accuracy effects in ISFG and IIFG, as well as a large cluster with an
568 overlapping Accuracy main effect in rIFG.

569 Figure 9 shows the activation pattern in two rIPL clusters for illustration
570 showing an increase in HbO and BOLD as the working memory load increased
571 from 2 to 6 items ($p < 0.05$).

572 For the comparison between HbR and BOLD, we found large clusters with
573 overlapping Load main effects in right superior occipital gyrus (rSOG) and right

574 postcentral gyrus. There was also a large cluster with an overlapping Load x Trial
575 x Accuracy interaction in the left angular gyrus (AG), and a large cluster with an
576 overlapping Accuracy main effect in IIFG. In Figure 10, we observed an increase
577 in BOLD and a decrease in HbR activation in the rSOG cluster (Load Main
578 effect) as the working memory load increased from 2 to 6 showing ($p < 0.05$).
579 Albeit, in different cortical areas, HbR activation in rSOG shows an opposite
580 trend to that of HbO and BOLD activation in rIPL.



■ Unique BOLD ANOVA effects
 ■ Unique HbO ANOVA effects
 ■ Unique HbR ANOVA effects
■ Overlap HbO-BOLD ANOVA effects
 ■ Overlap HbR-BOLD ANOVA effects

581
 582 Figure 8. Montage showing overlap between ANOVA effects from HbO and HbR concentration and percent BOLD signal change. Note that the
 583 spatial distributions have been masked to create binary images. The teal color indicates clusters with significant unique BOLD ANOVA effects;
 584 green color indicates clusters with significant unique HbO ANOVA effects; brown color indicates clusters with significant unique HbR ANOVA
 585 effects; pink color indicates clusters with significant overlap between HbO and BOLD ANOVA effects and red color indicates clusters with
 586 significant HbR-BOLD ANOVA effects. *Note that overlap between HbO, HbR and MRI accounted for only 15 voxels (summed across all cortical*
 587 *regions) and not shown in Figure 8.*

588 Table 1. Regions commonly activated by the main effects and interaction effects of Load,
 589 Accuracy and Trial for HbO and BOLD ANOVAs. *Note that, there were no common regions of*
 590 *overlap for the Trial main effect and the Accuracy X Trial interaction.*

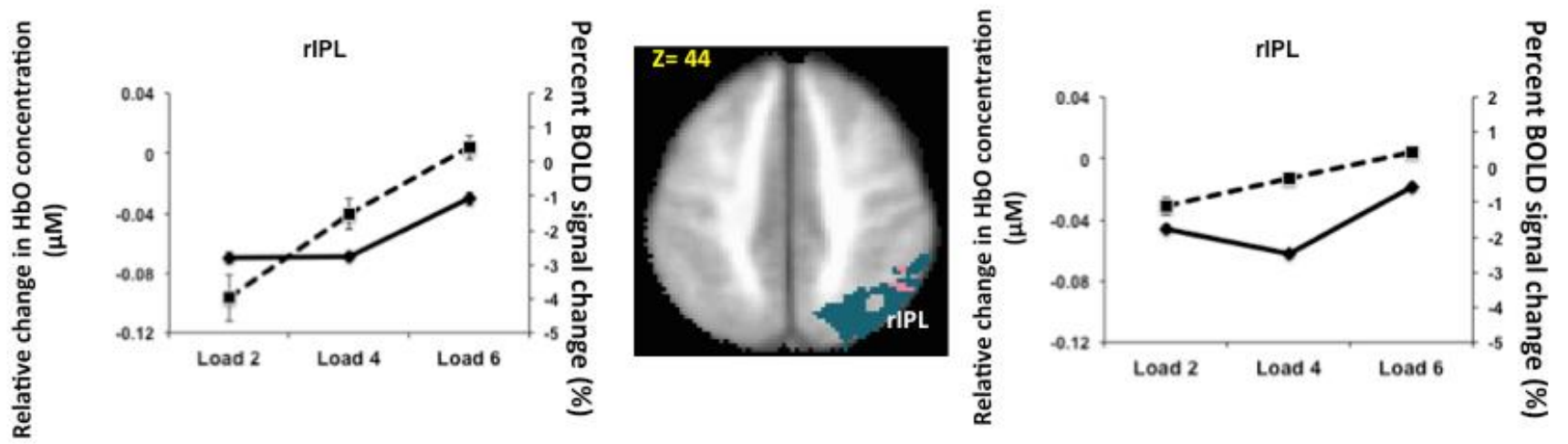
Region	Hemi	Center of Mass MNI Coordinates (LPI orientation)			Size (mm ³)
		x	y	z	
Load Main effect					
Inferior parietal lobule	R	50.8	-50.2	42.9	160
Inferior parietal lobule	R	50.3	-57	46.3	144
Middle frontal gyrus	R	37.1	45.9	11.6	824
Middle frontal gyrus	R	39.1	21.8	34.8	232
Middle frontal gyrus	R	38.5	56	12.5	64
Middle frontal gyrus	R	39.6	29.2	40	40
Middle frontal gyrus	R	38	57	0	16
Middle frontal gyrus	R	36	56	2	8
Middle frontal gyrus	R	42	46	20	8
Middle frontal gyrus	R	38	24	40	8
Load x Accuracy					
Superior frontal gyrus	L	-22.3	40.6	33.7	56
Superior frontal gyrus	L	-24.7	44.7	38	24
Superior frontal gyrus	L	-21.3	45.3	40	24
Superior frontal gyrus	L	-18	44	36	8
Load x Trial					
Postcentral gyrus	R	52	-5.8	27.8	80
Load x Trial x Accuracy					
Superior frontal gyrus	L	-14.9	54.3	27.4	224
Inferior frontal gyrus	L	-38.9	13.5	24.6	176
Inferior frontal gyrus	R	46	30	26	8
Inferior frontal gyrus	R	44	28	28	8
Accuracy Main effect					
Middle frontal gyrus	R	44	41	20	16
Middle frontal gyrus	R	44	32	22	8
Inferior frontal gyrus	R	46.7	30.4	19	448
Inferior frontal gyrus	R	42	29	24	16
Inferior frontal gyrus	R	40	32	14	8
Inferior frontal gyrus	R	44	36	16	8
Inferior frontal gyrus	R	40	26	24	8
Postcentral gyrus	R	54	-3	24	16

591

592 Table 2. Regions commonly activated by the main effects and interaction effects of Load,
 593 Accuracy and Trial for HbR and BOLD ANOVAs. *Note that, there were no common regions of*
 594 *overlap for Trial main effect and Accuracy x Trial interaction.*

Region	Hemi	Center of Mass MNI Coordinates (LPI orientation)			Size (mm ³)
		x	y	z	
Load Main effect					
Superior occipital gyrus	R	25.7	-75	38.5	568
Superior occipital gyrus	R	22	-78	42	8
Postcentral gyrus	R	54.4	-20.3	39.1	552
Load x Accuracy					
Superior temporal gyrus	R	63	-30	10	16
Load x Trial					
Inferior frontal gyrus	L	-52	36	4	8
Load x Trial x Accuracy					
Angular gyrus	L	-51.8	-60.4	35.1	88
Angular gyrus	L	-47	-58	30	16
Angular gyrus	L	-48	-60	32	8
Middle temporal gyrus	L	-61.2	-34.8	3.6	40
Middle temporal gyrus	L	-62	-30	2	8
Middle temporal gyrus	L	-64	-30	4	8
Accuracy Main effect					
Inferior frontal gyrus	L	-39.2	25.4	26.7	152
Supramarginal gyrus	R	58	-40	34	40
Middle temporal gyrus	L	-64	-42	8	24
Middle temporal gyrus	L	-60	-40	7	16
Middle temporal gyrus	L	-62	-40	4	8
Superior temporal gyrus	R	60	-16	0	8

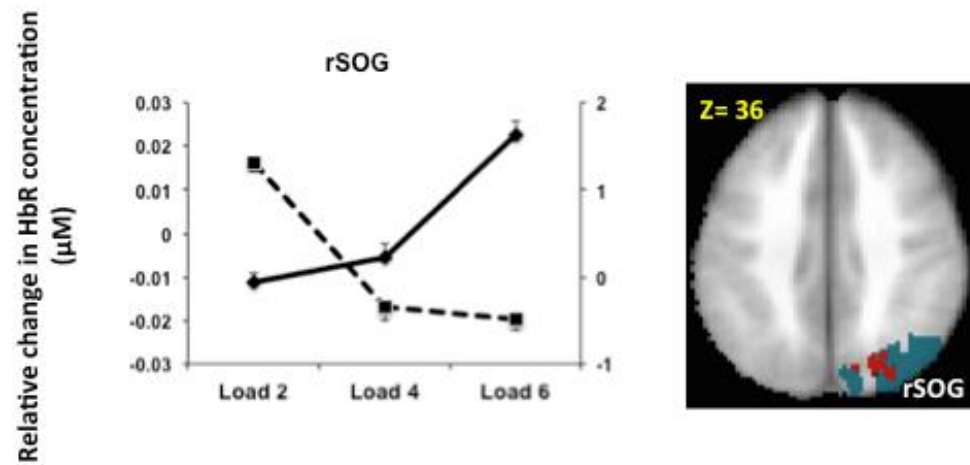
595
596



597

598

Figure 9. Main effect of Load in two rIPL clusters. Bold lines indicate BOLD activation and dashed lines indicate HbO activation.



599

600

Figure 10. Main effect of Load in a rSOG cluster. Bold lines indicate BOLD activation and dashed lines indicate HbR activation.

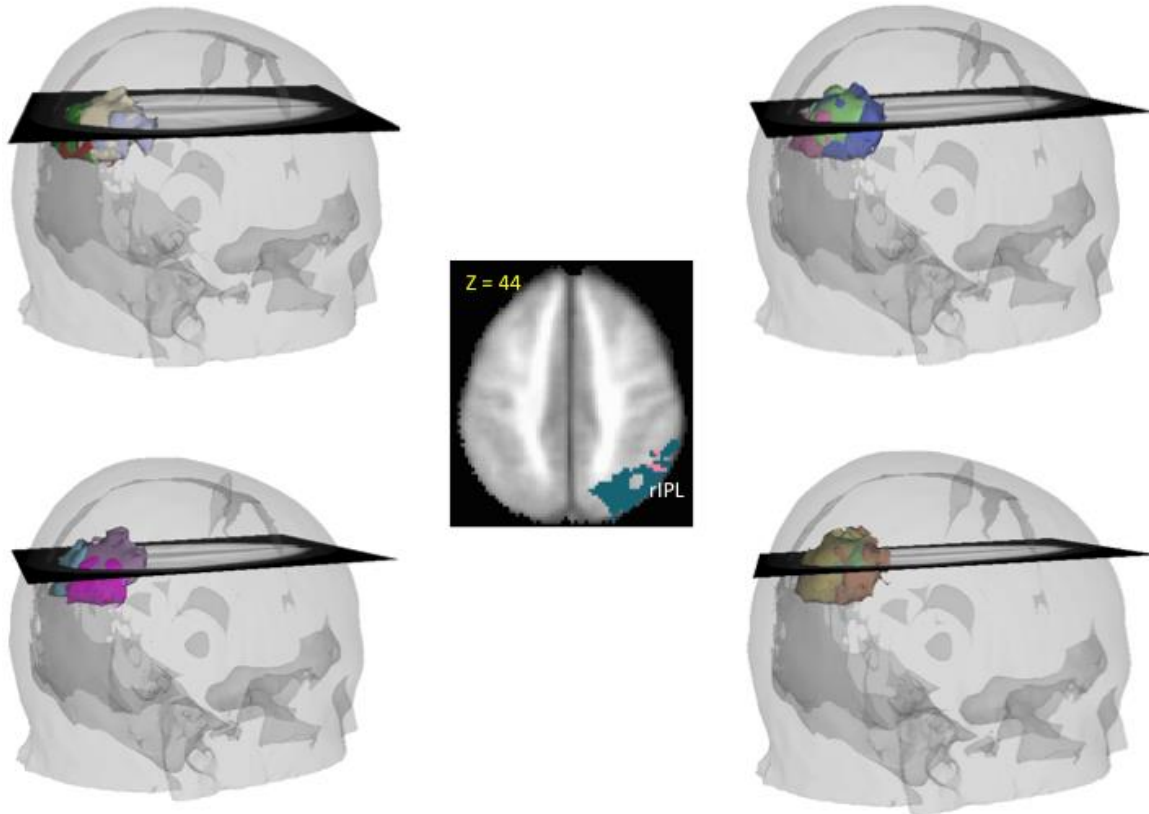
601 **4. Discussion**

602 The objective of the current study was to validate a novel methodological
603 pipeline to move fNIRS analyses from conventional channel-based analyses on
604 the surface of the head to voxel-based analyses within the brain volume. There
605 are several advantages of the image reconstruction approach. First, this
606 approach aligns the fNIRS data across participants, factoring in differences in
607 optode placement due to experimenter errors and/or movement of the
608 participant. The latter is likely to be a key source of variation when dealing with
609 infants, young children, and clinical populations who have difficulty sitting still.
610 Second, the image reconstruction approach can capitalize on cases where
611 nearby fNIRS channels record from overlapping cortical areas, potentially
612 boosting the strength of effects that are weak and distributed across channels.
613 Third, the image reconstruction approach allows for direct comparisons with fMRI
614 data. Finally, this approach facilitates analysis in that fMRI analysis tools can be
615 readily used with fNIRS data. This makes it easy to port advanced analysis
616 techniques from the fMRI literature to the fNIRS literature.

617 These advantages of the image reconstruction approach are evident in
618 Figure 11. In this figure, we show surface projections of the sensitivity volumes
619 for a single fNIRS channel across the 13 participants. The single channel's
620 positions across the 13 participants have been shown using the four 3D images
621 (top left image shows this channel placement on 4 participants and top right,
622 bottom left and right show this channel placement on 3 participants each). This
623 particular channel showed considerable variation in position on the head surface.
624 The image reflects the challenge of placing fNIRS optodes on the head relative to
625 the 10-20 system. Variation was likely introduced when we positioned
626 participants inside the scanner bore causing optodes to shift slightly as
627 participants laid down. Consequently, this channel was recording from different
628 parts of cortex across participants.

629 In stark contrast to this variable cloud on the brain surface, the image at
630 the center shows results within the brain volume underneath the region where
631 this fNIRS channel was placed. The cluster shows a significant main effect of

632 Load in the rIPL (obtained from Figure 9 – HbO-BOLD effect) from the image
633 reconstruction approach. The fNIRS cluster precisely overlaps with a localized
634 main effect of Load from the fMRI analysis. The fNIRS analysis was also
635 straightforward to conduct using an fMRI analyses toolbox such as AFNI.



636
637 Figure 11. Variations of a channel across 13 subjects (shown in multiple colors across the
638 different 3D images). Image at the center shows an axial slice for the Load effect (obtained from
639 Figure 9 – HbO-BOLD effects) in rIPL.

640

641 In the sections that follow, we elaborate on our validation findings. We
642 focus first on the correlational results. Next, we evaluate the multi-factorial
643 effects, highlighting results showing the parametric manipulation of the memory
644 load.

645

646 4.1. Correlations between fNIRS and fMRI

647 Previous concurrent fNIRS and fMRI studies have established that results
648 from both modalities are well-correlated across sensory tasks (Cui et al., 2011;
649 Gagnon et al., 2012; Huppert et al., 2006, 2005; Sassaroli et al., 2005; Sato et

650 al., 2013; Schroeter et al., 2006; Strangman et al., 2002; Wijekumar et al.,
651 2012a). However, there is less work that has examined the correspondence
652 between both techniques in cognitive tasks (for exceptions, see Cui et al., 2011;
653 Sato et al., 2013).

654 In the current study, fNIRS measures were correlated with BOLD
655 measures in a number of cortical regions that spanned the frontal, parietal,
656 temporal, and occipital cortices. There were both positive and negative
657 correlations between HbO and HbR and BOLD signals. Collectively, positive
658 HbR-BOLD correlations were more frequent than positive HbO-BOLD
659 correlations. Interestingly, there is debate on the exact role of HbR during
660 experimental tasks, an issue which is spurred on by studies showing strong
661 correlations between HbR and BOLD (Huppert et al., 2006, 2005; Kleinschmidt et
662 al., 1996; MacIntosh et al., 2003; Mehagnoul-Schipper et al., 2002; Murata and
663 Sakatani, 2002; Sato et al., 2013; Siegel et al., 2003; Toronov et al., 2001). Other
664 studies, by contrast, have shown higher correlations between HbO and BOLD
665 (Cui et al., 2011; Heinzl et al., 2013; Hoshi and Tamura, 1993; Strangman et al.,
666 2002; Yamamoto and Kato, 2002), and a few studies have reported significant
667 correlations between total hemoglobin concentration and BOLD (e.g., Hess et al.,
668 2000). These findings highlight the need for clarity on precisely how HbO, HbR,
669 and BOLD are related.

670 There is also a need for clarity on what negative correlations between
671 HbO and BOLD and HbR and BOLD represent. A few studies have reported that
672 signals obtained from fNIRS are sensitive to microvasculature such as arterioles
673 and venules instead of larger vasculature such as arteries and veins as the light
674 is unlikely to be detected back at the scalp in the latter case (Boushel et al.,
675 2001; Cannestra et al., 2001; Liu et al., 1995a, 1995b; Schroeter et al., 2006). In
676 On the other hand, fMRI is likely to be more sensitive to bigger vessels. These
677 anatomical differences taken within the context of a time and space-sensitive
678 neural process like VWM, could explain the presence of negative correlations
679 between modalities. Future validation studies that use cognitive tasks could

680 examine both spatial and temporal aspects of these signals to better understand
681 the relationship between HbO, HbR, and BOLD.

682 How do previous reports of correlations between fNIRS and fMRI compare
683 with those reported in the current study? Cui et al. (2011) projected a marker
684 from each channel from the scalp to the brain and correlated an average as well
685 as voxel-wise BOLD signals from a 5mm radius of the projected points with that
686 specific channel's fNIRS signal (Cui et al., 2011). They showed good spatial
687 correspondence between fMRI and fNIRS across the frontal and parietal cortices
688 in response to an n-back visual working memory task. They found that the
689 highest correlation between HbO and BOLD was 0.26 and the HbR and BOLD
690 was 0.23. An earlier study by Okamoto and colleagues observed almost equal
691 correlation values between HbO and BOLD and HbR and BOLD during an apple-
692 peeling exercise (Okamoto et al., 2004). Further, they found that the highest
693 correlations were observed in the middle frontal and inferior parietal areas.
694 Overall, these results are in agreement with findings from the current study
695 wherein the highest correlations were observed in SPL and IFG. That said, we
696 observe much higher correlations between fNIRS and fMRI activation than
697 shown in previous studies.

698 An interesting observation from the correlation scatterplots was that the
699 variation in the fNIRS signal was greater for SPL than for IFG. The frontal cortex
700 is responsible for the maintenance of goals and abstract representations of the
701 task whereas parietal regions are responsible for feature-processing and visual
702 stimulus encoding (D'Esposito and Postle, 2015). Given these functions, it is
703 possible that increased variability in SPL might be a reflection of inter-individual
704 differences in stimulus processing. Future work will need to explore the extent to
705 which variations in brain activation might reflect inter-individual differences in
706 performance.

707 In another study, Sato et al. used photon path distributions to weight
708 averaged BOLD signals from grey matter voxels and correlated those with fNIRS
709 signals in the channels that 'supervised' those voxels (Sato et al., 2013). They
710 conducted correlations between time-domain signals and found that HbR was

711 marginally more correlated with BOLD than HbO. They reported that the middle
712 of prefrontal cortex, around the inferior parietal and superior temporal cortices
713 showed a high correlation between BOLD and fNIRS signals. In the current
714 study, we found that both positive HbO-BOLD and HbR-BOLD showed similar
715 ranges of correlations. Further, the number of correlated voxels for HbR-BOLD
716 was slightly higher than for HbO-BOLD.

717 Another interesting metric that has been reported in previous studies is the
718 depth at which these correlations have been observed. Schoreter et al. (2006)
719 found that the highest correlations between fNIRS and fMRI signals in response
720 to visual stimulation occurred between 15-20 mm from surface of the scalp
721 (Schroeter et al., 2006). Cui et al. (2011) observed that peak correlations were
722 observed at a depth of 4 voxels, which translated to approximately 16 mm [as per
723 the voxel size they specified] (Cui et al., 2011). In the current study, voxels with
724 the highest correlations within each cluster were observed at a mean depth of 8.8
725 mm of the *cortical surface*. Taken together with previously reported measures of
726 scalp and skull thickness estimates of about 11-13 mm (Oldendorf WH, 1969;
727 Strangman et al., 2014), our findings are in agreement with previous studies.

728 To summarize, both HbO and HbR were positively correlated with BOLD
729 in regions within the VWM network. These correlations were much higher in
730 magnitude but at a similar cortical depth as findings reported in previous studies.
731 This is an important finding given that there have been relatively few validation
732 studies using cognitive tasks and no previous validation studies using the image
733 reconstruction approach described in the present report. Although promising,
734 future work will be needed to more understand the nature of the correlations
735 (positive and negative) observed across neuroimaging modalities.

736

737 4.2. Multi-factorial effects of VWM

738 In addition to voxel-wise correlations across modalities, we examined
739 whether task-specific effects were also consistent in both the fNIRS and fMRI
740 data. To examine this question, we intersected effects from BOLD, HbO, and
741 HbR ANOVAs. We found overlapping effects across parts of the VWM network

742 as reported in previous fMRI studies (Linden et al., 2003; Luck and Vogel, 2013;
743 Ma et al., 2014; Pessoa et al., 2002; Postle, 2015; Todd and Marois, 2004; Todd
744 et al., 2005). These findings are also consistent with previous fNIRS studies that
745 have investigated VWM, albeit using different analytical methods (Aoki et al.,
746 2011; Cui et al., 2011; Cutini et al., 2011; McKendrick et al., 2014; Ogawa et al.,
747 2014; Sato et al., 2013; Tsujimoto et al., 2004).

748 We found fNIRS and fMRI effects within regions of the frontal cortex that
749 are important to VWM processing, including MFG. The MFG has been implicated
750 in a number of VWM studies as a key site for the maintenance of rules, goals,
751 and abstract representations that can guide other parts of the VWM network
752 (Aoki et al., 2011; Barbey et al., 2013; Haxby et al., 2000; Munk et al., 2002;
753 Pessoa and Ungerleider, 2004; Pessoa et al., 2002; Sala and Courtney, 2007;
754 Sala et al., 2003; Sala-Llonch et al., 2012; Smith and Jonides, 1998).

755 Further, we also found robust fNIRS and fMRI activation in the IPL that
756 increased with increasing working memory load. Our results are in agreement
757 with Todd and Marois who showed that the activation in the inferior parietal
758 sulcus increased with an increase in working memory load (Todd and Marois,
759 2004). Furthermore, Xu et al (2006) proposed that the inferior IPS is responsible
760 for processing spatial information using a spatial indexing mechanism whereas
761 LOC and superior IPS are important in processing object complexity (Xu and
762 Chun, 2006). Similarly, Shahfritz et al (2006) showed that regions engaged in
763 spatial attention were activated when objects were presented simultaneously as
764 opposed to presented sequentially suggesting a link between spatial attention
765 and feature binding (Shafritz and Gore, 2002). In our experiment, we only
766 manipulated the color of the stimuli; however, it is plausible that the parietal
767 activation we observed reflects a type of spatial indexing critical to feature
768 binding.

769 Interestingly, the fNIRS ANOVA effects were focal in comparison to the
770 effects from the BOLD ANOVA. We applied a liberal threshold of $p < 0.05$ to our
771 fMRI data relative to previous studies in an effort to maintain consistency across
772 both approaches. However, it is possible that the fMRI signal requires a more

773 stringent threshold; much like that demonstrated in previous fMRI studies to
774 show more focal effects. Clusters of activation after more stringent thresholding
775 might be due to the fMRI technique, capturing certain aspects of the task that
776 fNIRS could not. The current study is the first attempt at utilizing an ANOVA
777 approach based on voxel-based fNIRS measures to compare activation with
778 BOLD spatial distributions. We believe that more studies will need to be
779 conducted to explore this novel finding.

780 Recent studies have discussed the importance of reporting both HbO and
781 HbR effects to clarify what fNIRS signals can tell us about brain function
782 (Tachtsidis and Scholkmann, 2016; Zhang et al., 2016). These studies also
783 advocate removing systemic effects from cerebral and extra-cerebral signals,
784 thereby leaving only task-relevant neural activation. For instance, Zhang et al.
785 found that after removing global effects from the acquired signal, task-based
786 HbO and HbR waveforms were more temporally and spatially consistent with
787 each other. Indeed, this result was based on the assumption that true, task-
788 related activation requires consistency between HbO and HbR signals. Critically,
789 they applied their global signal correction on waveforms obtained from a block
790 design of a finger-thumb tapping task. It will be important in future work to
791 investigate whether these methods extend to event-related designs in cognitive
792 tasks. In this context, we note that in the current study, we observed VWM
793 effects amongst overlapping *and* non-overlapping regions of HbO, HbR and
794 BOLD activation.

795 In addition to the removal of global systemic effects, it may be possible in
796 the future to work to isolate HbO and HbR effects with a different experimental
797 design. In the present study, we used relatively brief presentation times and short
798 delays to mimic previous studies; however, longer delays might help isolate
799 distinctive HbO and HbR patterns. For instance, several fMRI studies have
800 explored neural activation patterns across the encoding, maintenance, and
801 comparison phases by lengthening the duration of each phase (Linden et al.,
802 2003; Todd & Marois, R., 2005). Such tasks might be useful in teasing apart the

803 complicated dynamics between cerebral blood flow, cerebral blood volume, and
804 oxygen consumption.

805 In conclusion, findings from the present study successfully extend
806 previous work, validating a novel methodological pipeline to move fNIRS
807 analyses from the conventional channel-space to voxel-space within the volume
808 of the brain. Results show fNIRS and fMRI are correlated across key VWM
809 regions in the fronto-parietal network. Further, both modalities show spatial
810 overlap in those clusters that are activated in response to parametric
811 manipulations of the task including increasing working memory load. Most
812 critically, we have demonstrated that the image-based fNIRS approach can
813 effectively translate fNIRS signals into voxel space to enable direct comparison
814 with fMRI results.

815

816 **Acknowledgements**

817 We would like to thank David A. Boas for his valuable input on this paper.

818

819 JPS acknowledges support from NSF BCS1029082.

820

821

822 **References**

- 823 Aoki, R., Sato, H., Katura, T., Utsugi, K., Koizumi, H., Matsuda, R., Maki, A.,
824 2011. Relationship of negative mood with prefrontal cortex activity during
825 working memory tasks: An optical topography study. *Neurosci. Res.* 70,
826 189–196. doi:10.1016/j.neures.2011.02.011
- 827 Barbey, A.K., Koenigs, M., Grafman, J., 2013. Dorsolateral prefrontal
828 contributions to human working memory. *Cortex* 49, 1195–1205.
829 doi:10.1016/j.cortex.2012.05.022
- 830 Boas, D. a., Elwell, C.E., Ferrari, M., Taga, G., 2014. Twenty years of functional
831 near-infrared spectroscopy: Introduction for the special issue. *Neuroimage*
832 85, 1–5. doi:10.1016/j.neuroimage.2013.11.033
- 833 Bortfeld, H., Fava, E., Boas, D. a, 2009. Identifying cortical lateralization of
834 speech processing in infants using near-infrared spectroscopy. *Dev.*
835 *Neuropsychol.* 34, 52–65. doi:10.1080/87565640802564481
- 836 Bortfeld, H., Wruck, E., Boas, D. a., 2007. Assessing infants' cortical response to
837 speech using near-infrared spectroscopy. *Neuroimage* 34, 407–15.
838 doi:10.1016/j.neuroimage.2006.08.010
- 839 Boushel, R., Langberg, H., Olesen, J., Gonzales-Alonzo, J., Bülow, J., Kjaer, M.,
840 2001. Monitoring tissue oxygen availability with near infrared spectroscopy
841 (NIRS) in health and disease. *Scand. J. Med. Sci. Sports* 11, 213–222.
842 doi:DOI 10.1034/j.1600-0838.2001.110404.x
- 843 Brigadoi, S., Cutini, S., Scarpa, F., Scatturin, P., Dell'Acqua, R., 2012. Exploring
844 the role of primary and supplementary motor areas in simple motor tasks
845 with fNIRS. *Cogn. Process.* 13, 97–101. doi:10.1007/s10339-012-0446-z
- 846 Brigadoi, S., Powell, S., Cooper, R.J., Dempsey, L.A., Arridge, S., Everdell, N.,
847 Hebden, J., Gibson, A.P., 2015. Evaluating real-time image reconstruction in
848 diffuse optical tomography using physiologically realistic test data. *Biomed.*
849 *Opt. Express* 6, 4719. doi:10.1364/BOE.6.004719
- 850 Calvetti, D., Morigi, S., Reichel, L., Sgallari, F., 2000. Tikhonov regularization and
851 the L-curve for large discrete ill-posed problems. *J. Comput. Appl. Math.*
852 123, 423–446. doi:10.1016/S0377-0427(00)00414-3

853 Cannestra, a F., Pouratian, N., Bookheimer, S.Y., Martin, N. a, Beckerand, D.P.,
854 Toga, a W., 2001. Temporal spatial differences observed by functional MRI
855 and human intraoperative optical imaging. *Cereb. Cortex* 11, 773–82.
856 doi:10.1093/cercor/11.8.773

857 Cooper, R.J., Caffini, M., Dubb, J., Fang, Q., Custo, A., Tsuzuki, D., Fischl, B.,
858 Wells, W., Dan, I., Boas, D., 2012. Validating atlas-guided DOT: a
859 comparison of diffuse optical tomography informed by atlas and subject-
860 specific anatomies. *Neuroimage* 62, 1999–2006.
861 doi:10.1016/j.neuroimage.2012.05.031

862 Cui, X., Bray, S., Bryant, D.M., Glover, G.H., Reiss, A.L., 2011. A quantitative
863 comparison of NIRS and fMRI across multiple cognitive tasks. *Neuroimage*
864 54, 2808–2821. doi:10.1016/j.neuroimage.2010.10.069

865 Cutini, S., Scarpa, F., Scatturin, P., Jolicoeur, P., Pluchino, P., Zorzi, M.,
866 Dell’Acqua, R., 2011. A hemodynamic correlate of lateralized visual short-
867 term memories. *Neuropsychologia* 49, 1611–21.
868 doi:10.1016/j.neuropsychologia.2010.12.009

869 D’Esposito, M., Postle, B.R., 2015. The Cognitive Neuroscience of Working
870 Memory. *Annu. Rev. Psychol.* 66, 186–219.
871 doi:10.1093/acprof:oso/9780198570394.001.0001

872 Druzgal, T.J., D’Esposito, M., 2003. Dissecting contributions of prefrontal cortex
873 and fusiform face area to face working memory. *J. Cogn. Neurosci.* 15, 771–
874 784. doi:10.1162/089892903322370708

875 Emir, U.E., Ozturk, C., Akin, a, 2008. Multimodal investigation of fMRI and fNIRS
876 derived breath hold BOLD signals with an expanded balloon model. *Physiol.*
877 *Meas.* 29, 49–63. doi:10.1088/0967-3334/29/1/004

878 Erdoğan, S.B., Yücel, M.A., Akın, A., 2014. Analysis of task-evoked systemic
879 interference in fNIRS measurements: Insights from fMRI. *Neuroimage* 87,
880 490–504. doi:10.1016/j.neuroimage.2013.10.024

881 Fabiani, M., Gordon, B.A., Maclin, E.L., Pearson, M.A., Brumback-Peltz, C.R.,
882 Low, K.A., McAuley, E., Sutton, B.P., Kramer, A.F., Gratton, G., 2014.
883 Neurovascular coupling in normal aging: A combined optical, ERP and fMRI

884 study. *Neuroimage* 85, 592–607. doi:10.1016/j.neuroimage.2013.04.113
885 Fang, Q., Boas, D. a., 2009. Monte Carlo simulation of photon migration in 3D
886 turbid media accelerated by graphics processing units. *Opt. Express* 17,
887 20178–20190. doi:10.1364/OE.17.020178
888 Ferrari, M., Quaresima, V., 2012. A brief review on the history of human
889 functional near-infrared spectroscopy (fNIRS) development and fields of
890 application. *Neuroimage* 63, 921–935.
891 doi:10.1016/j.neuroimage.2012.03.049
892 Fishburn, F.A., Norr, M.E., Medvedev, A. V., Vaidya, C.J., 2014. Sensitivity of
893 fNIRS to cognitive state and load. *Front. Hum. Neurosci.* 8, 1–11.
894 doi:10.3389/fnhum.2014.00076
895 Gagnon, L., Yücel, M. a., Dehaes, M., Cooper, R.J., Perdue, K.L., Selb, J.,
896 Huppert, T.J., Hoge, R.D., Boas, D. a., 2012. Quantification of the cortical
897 contribution to the NIRS signal over the motor cortex using concurrent NIRS-
898 fMRI measurements. *Neuroimage* 59, 3933–3940.
899 doi:10.1016/j.neuroimage.2011.10.054
900 Haxby, J. V, Petit, L., Ungerleider, L.G., Courtney, S.M., 2000. Distinguishing the
901 functional roles of multiple regions in distributed neural systems for visual
902 working memory. *Neuroimage* 11, 380–91. doi:10.1006/nimg.2000.0592
903 Heinzl, S., Haeussinger, F.B., Hahn, T., Ehlis, A.-C., Plichta, M.M., Fallgatter,
904 A.J., 2013. Variability of (functional) hemodynamics as measured with
905 simultaneous fNIRS and fMRI during intertemporal choice. *Neuroimage* 71,
906 125–134. doi:10.1016/j.neuroimage.2012.12.074
907 Hess, a, Stiller, D., Kaulisch, T., Heil, P., Scheich, H., 2000. New insights into
908 the hemodynamic blood oxygenation level-dependent response through
909 combination of functional magnetic resonance imaging and optical recording
910 in gerbil barrel cortex. *J. Neurosci.* 20, 3328–38.
911 Hoshi, Y., Tamura, M., 1993. Dynamic multichannel near-infrared optical imaging
912 of human brain activity. *J Appl.Physiol* 75, 1842–1846.
913 Huppert, T.J., Hoge, R.D., Diamond, S.G., Franceschini, M.A., Boas, D.A., 2006.
914 A temporal comparison of BOLD, ASL, and NIRS hemodynamic responses

915 to motor stimuli in adult humans. *Neuroimage* 29, 368–82.
916 doi:10.1016/j.neuroimage.2005.08.065

917 Huppert, T.J., Hoge, R.D., Franceschini, M.A., Boas, D.A., 2005. *A*
918 spatial-temporal comparison of fMRI and NIRS hemodynamic responses to
919 motor stimuli in adult humans*</i>*; 5693, 191–202.
920 doi:10.1117/12.612143

921 Kleinschmidt, a, Obrig, H., Requardt, M., Merboldt, K.D., Dirnagl, U., Villringer,
922 a, Frahm, J., 1996. Simultaneous recording of cerebral blood oxygenation
923 changes during human brain activation by magnetic resonance imaging and
924 near-infrared spectroscopy. *J. Cereb. Blood Flow Metab.* 16, 817–26.
925 doi:10.1097/00004647-199609000-00006

926 Learmonth, A.E., Newcombe, N.S., Huttenlocher, J., 2001. Toddlers' use of
927 metric information and landmarks to reorient. *J. Exp. Child Psychol.* 80, 225–
928 244.

929 Li, A., Zhang, Q., Culver, J.P., Miller, E.L., Boas, D. a, 2004. Reconstructing
930 chromosphere concentration images directly by continuous-wave diffuse
931 optical tomography. *Opt. Lett.* 29, 256–258. doi:10.1364/OL.29.000256

932 Linden, D.E.J., Bittner, R.A., Muckli, L., Waltz, J.A., Kriegeskorte, N., Goebel, R.,
933 Singer, W., Munk, M.H.J., 2003. Cortical capacity constraints for visual
934 working memory: dissociation of fMRI load effects in a fronto-parietal
935 network. *Neuroimage* 20, 1518–1530.
936 doi:10.1016/j.neuroimage.2003.07.021

937 Liu, H., Boas, D. a, Zhang, Y., Yodh, a G., Chance, B., 1995a. Determination of
938 optical properties and blood oxygenation in tissue using continuous NIR
939 light. *Phys. Med. Biol.* 40, 1983–1993. doi:10.1088/0031-9155/40/11/015

940 Liu, H., Chance, B., Hielscher, a H., Jacques, S.L., Tittel, F.K., 1995b. Influence
941 of blood vessels on the measurement of hemoglobin oxygenation as
942 determined by time-resolved reflectance spectroscopy. *Med. Phys.*
943 doi:10.1118/1.597520

944 Logothetis N.K. Augath M., Trinath T., Oeltermann A, P.J., 2001.
945 Neurophysiological investigation of the basis of the fMRI signal. . *Nature*

946 412, 150–157.

947 Luck, S., Vogel, E., 1997. The capacity of visual working memory for features
948 and conjunctions. *Nature* 390, 279–281.

949 Luck, S.J., Vogel, E.K., 2013. Visual working memory capacity: from
950 psychophysics and neurobiology to individual differences. *Trends Cogn. Sci.*
951 17, 391–400. doi:10.1016/j.tics.2013.06.006

952 Ma, W.J., Husain, M., Bays, P.M., 2014. Changing concepts of working memory.
953 *Nat. Neurosci.* 17, 347–356. doi:10.1038/nn.3655

954 MacIntosh, B.J., Klassen, L.M., Menon, R.S., 2003. Transient hemodynamics
955 during a breath hold challenge in a two part functional imaging study with
956 simultaneous near-infrared spectroscopy in adult humans. *Neuroimage* 20,
957 1246–1252. doi:10.1016/S1053-8119(03)00417-8

958 Maggioni, E., Molteni, E., Zucca, C., Reni, G., Cerutti, S., Triulzi, F.M., Arrigoni,
959 F., Bianchi, A.M., 2015. Investigation of negative BOLD responses in human
960 brain through NIRS technique. A visual stimulation study. *Neuroimage* 108,
961 410–422. doi:10.1016/j.neuroimage.2014.12.074

962 McKendrick, R., Ayaz, H., Olmstead, R., Parasuraman, R., 2014. Enhancing
963 dual-task performance with verbal and spatial working memory training:
964 Continuous monitoring of cerebral hemodynamics with NIRS. *Neuroimage*
965 85, 1014–1026. doi:10.1016/j.neuroimage.2013.05.103

966 Mehagnoul-Schipper, D.J., van der Kallen, B.F.W., Colier, W.N.J.M., van der
967 Sluijs, M.C., van Erning, L.J.T.O., Thijssen, H.O.M., Oeseburg, B.,
968 Hoefnagels, W.H.L., Jansen, R.W.M.M., 2002. Simultaneous measurements
969 of cerebral oxygenation changes during brain activation by near-infrared
970 spectroscopy and functional magnetic resonance imaging in healthy young
971 and elderly subjects. *Hum. Brain Mapp.* 16, 14–23. doi:10.1002/hbm.10026

972 Molteni, E., Butti, M., Bianchi, A.M., Reni, G., 2008. Activation of the prefrontal
973 cortex during a visual n-back working memory task with varying memory
974 load: a near infrared spectroscopy study. *Conf. Proc. IEEE Eng. Med. Biol.*
975 *Soc.* 2008, 4024–7. doi:10.1109/IEMBS.2008.4650092

976 Munk, M.H.J., Linden, D.E.J., Muckli, L., Lanfermann, H., Zanella, F.E., Singer,

977 W., Goebel, R., 2002. Distributed cortical systems in visual short-term
978 memory revealed by event-related functional magnetic resonance imaging.
979 Cereb. Cortex 12, 866–876. doi:10.1093/cercor/12.8.866

980 Murata, Y., Sakatani, K., 2002. Increase in focal concentration of
981 deoxyhaemoglobin during neuronal activity in cerebral ischaemic patients. J.
982 Neurol. ... 73, 182–184. doi:10.1136/jnnp.73.2.182

983 Muthalib, M., Anwar, A.R., Perrey, S., Dat, M., Galka, A., Wolff, S., Heute, U.,
984 Deuschl, G., Raethjen, J., Muthuraman, M., 2013. Multimodal integration of
985 fNIRS, fMRI and EEG neuroimaging. Clin. Neurophysiol. 124, 2060–2062.
986 doi:10.1016/j.clinph.2013.03.018

987 Ogawa, Y., Kotani, K., Jimbo, Y., 2014. Relationship between working memory
988 performance and neural activation measured using near-infrared
989 spectroscopy. Brain Behav. 4, 544–51. doi:10.1002/brb3.238

990 Okamoto, M., Dan, H., Shimizu, K., Takeo, K., Amita, T., Oda, I., Konishi, I.,
991 Sakamoto, K., Isobe, S., Suzuki, T., Kohyama, K., Dan, I., 2004. Multimodal
992 assessment of cortical activation during apple peeling by NIRS and fMRI.
993 Neuroimage 21, 1275–1288. doi:10.1016/j.neuroimage.2003.12.003

994 Oldendorf WH, I.Y., 1969. Interference of scalp and skull with external
995 measurements of brain isotope content. 1. Isotope content of scalp and
996 skull. J Nucl Med 10:, 177–183.

997 Perlman, S.B., Huppert, T.J., Luna, B., 2015. Functional Near-Infrared
998 Spectroscopy Evidence for Development of Prefrontal Engagement in
999 Working Memory in Early Through Middle Childhood. Cereb. Cortex 1–10.
1000 doi:10.1093/cercor/bhv139

1001 Pessoa, L., Gutierrez, E., Bandettini, P., Ungerleider, L., 2002. Neural correlates
1002 of visual working memory: fMRI amplitude predicts task performance.
1003 Neuron 35, 975–87.

1004 Pessoa, L., Ungerleider, L.G., 2004. Neural Correlates of Change Detection and
1005 Change Blindness in a Working Memory Task — Cereb Cortex. Cereb.
1006 Cortex 14, 511–20. doi:10.1093/cercor/bhh013

1007 Pflieger, M.E., Barbour, R.L., 2012. Multimodal Integration of fMRI, EEG, and

1008 NIRS. Biomed. Opt. 3-D Imaging BSu2A.1.
1009 doi:10.1364/BIOMED.2012.BSu2A.1

1010 Postle, B.R., 2015. The cognitive neuroscience of visual short-term memory.
1011 Curr. Opin. Behav. Sci. 1, 40–46. doi:10.1016/j.cobeha.2014.08.004

1012 Rypma, B., Berger, J.S., D’Esposito, M., 2002. The influence of working-memory
1013 demand and subject performance on prefrontal cortical activity. J. Cogn.
1014 Neurosci. 14, 721–731. doi:10.1162/08989290260138627

1015 Sakatani, K., Murata, Y., Fujiwara, N., Hoshino, T., Nakamura, S., Kano, T.,
1016 Katayama, Y., 2013. Comparison of blood-oxygen-level-dependent
1017 functional magnetic resonance imaging and near-infrared spectroscopy
1018 recording during functional brain activation in patients with stroke and brain
1019 tumors. J. Biomed. Opt. 12, 062110. doi:10.1117/1.2823036

1020 Sala, J.B., Courtney, S.M., 2007. Binding of what and where during working
1021 memory maintenance. Cortex. 43, 5–21. doi:10.1016/S0010-9452(08)70442-
1022 8

1023 Sala, J.B., Rämä, P., Courtney, S.M., 2003. Functional topography of a
1024 distributed neural system for spatial and nonspatial information maintenance
1025 in working memory. Neuropsychologia 41, 341–356. doi:10.1016/S0028-
1026 3932(02)00166-5

1027 Sala-Llonch, R., Peña-Gómez, C., Arenaza-Urquijo, E.M., Vidal-Piñeiro, D.,
1028 Bargalló, N., Junqué, C., Bartrés-Faz, D., 2012. Brain connectivity during
1029 resting state and subsequent working memory task predicts behavioural
1030 performance. Cortex 48, 1187–1196. doi:10.1016/j.cortex.2011.07.006

1031 Sassaroli, A., Tonga, Y., Frederickb, B.B., Renshawb, P.F., Ehrenberga, B.L.,
1032 Fantinia, S., 2005. Studying brain function with concurrent near-infrared
1033 spectroscopy (NIRS) and functional magnetic resonance imaging (fMRI).
1034 Proc. SPIE 5693, 161–165. doi:10.1117/12.588422

1035 Sato, H., Yahata, N., Funane, T., Takizawa, R., Katura, T., Atsumori, H.,
1036 Nishimura, Y., Kinoshita, A., Kiguchi, M., Koizumi, H., Fukuda, M., Kasai, K.,
1037 2013. A NIRS–fMRI investigation of prefrontal cortex activity during a
1038 working memory task. Neuroimage 83, 158–173.

1039 doi:10.1016/j.neuroimage.2013.06.043
1040 Schroeter, M.L., Kupka, T., Mildner, T., Uludağ, K., Von Cramon, D.Y., 2006.
1041 Investigating the post-stimulus undershoot of the BOLD signal - A
1042 simultaneous fMRI and fNIRS study. *Neuroimage* 30, 349–358.
1043 doi:10.1016/j.neuroimage.2005.09.048
1044 Shafritz, K.M., Gore, J.C., 2002. The role of the parietal cortex in. *PNAS* 99,
1045 10917–10922.
1046 Siegel, A.M., Culver, J.P., Mandeville, J.B., Boas, D. a, 2003. Temporal
1047 comparison of functional brain imaging with diffuse optical tomography and
1048 fMRI during rat forepaw stimulation. *Phys. Med. Biol.* 48, 1391–1403.
1049 doi:10.1088/0031-9155/48/10/311
1050 Smith, E.E., Jonides, J., 1998. Neuroimaging analyses of human working
1051 memory. *Proc. Natl. Acad. Sci. USA* 95, 12061–12068. doi:VL - 95
1052 Steinbrink, J., Villringer, A., Kempf, F., Haux, D., Boden, S., Obrig, H., 2006.
1053 Illuminating the BOLD signal: combined fMRI-fNIRS studies. *Magn. Reson.*
1054 *Imaging* 24, 495–505. doi:10.1016/j.mri.2005.12.034
1055 Strangman, G., Culver, J.P., Thompson, J.H., Boas, D. a., 2002. A quantitative
1056 comparison of simultaneous BOLD fMRI and NIRS recordings during
1057 functional brain activation. *Neuroimage* 17, 719–731. doi:10.1016/S1053-
1058 8119(02)91227-9
1059 Strangman, G.E., Zhang, Q., Li, Z., 2014. Scalp and skull influence on near
1060 infrared photon propagation in the Colin27 brain template. *Neuroimage* 85,
1061 136–149. doi:10.1016/j.neuroimage.2013.04.090
1062 Tachtsidis, I., Scholkmann, F., 2016. False positives and false negatives in
1063 functional near-infrared spectroscopy: issues, challenges, and the way
1064 forward. *Neurophotonics* 3, 031405. doi:10.1117/1.NPh.3.3.031405
1065 Tanaka, H., Katura, T., Sato, H., 2014. Task-related oxygenation and cerebral
1066 blood volume changes estimated from NIRS signals in motor and cognitive
1067 tasks. *Neuroimage* 94, 107–119. doi:10.1016/j.neuroimage.2014.02.036
1068 Tikhonov A., 1963. Solution of Incorrectly Formulated Problems and the
1069 Regularization Method. *Sov. Math. Dokl.* 5, 1035/1038.

1070 Todd & Marois, R., J.J., 2005. Posterior parietal cortex activity predicts individual
1071 differences in visual short-term memory capacity. *Cogn. Affect. Behav.*
1072 *Neurosci.* 5, 144–155.

1073 Todd, J.J., Fougny, D., Marois, R., 2005. Visual short-term memory load
1074 suppresses temporo-parietal junction activity and induces inattentive
1075 blindness. *Psychol. Sci.* 16, 965–72. doi:10.1111/j.1467-9280.2005.01645.x

1076 Todd, J.J., Marois, R., 2004. Capacity limit of visual short-term memory in human
1077 posterior parietal cortex. *Nature* 428, 751–754.

1078 Tong, Y., Frederick, B. deB., 2012. Concurrent fNIRS and fMRI processing allows
1079 independent visualization of the propagation of pressure waves and bulk
1080 blood flow in the cerebral vasculature. *Neuroimage* 61, 1419–1427.
1081 doi:10.1016/j.neuroimage.2012.03.009

1082 Toronov, V., Webb, a, Choi, J.H., Wolf, M., Michalos, a, Gratton, E., Hueber, D.,
1083 2001. Investigation of human brain hemodynamics by simultaneous near-
1084 infrared spectroscopy and functional magnetic resonance imaging. *Med.*
1085 *Phys.* 28, 521–527. doi:10.1118/1.1354627

1086 Tsujimoto, S., Yamamoto, T., Kawaguchi, H., Koizumi, H., Sawaguchi, T., 2004.
1087 Prefrontal cortical activation associated with working memory in adults and
1088 preschool children: An event-related optical topography study. *Cereb.*
1089 *Cortex.* doi:10.1093/cercor/bhh030

1090 Tsuzuki, D., Dan, I., 2014. Spatial registration for functional near-infrared
1091 spectroscopy: From channel position on the scalp to cortical location in
1092 individual and group analyses. *Neuroimage.*
1093 doi:10.1016/j.neuroimage.2013.07.025

1094 Wijekumar, S., Shahani, U., McCulloch, D.L., Simpson, W. a., 2012a. Neural
1095 and vascular responses to fused binocular stimuli: A VEP and fNIRS study.
1096 *Investig. Ophthalmol. Vis. Sci.* 53, 5881–5889. doi:10.1167/iovs.12-10399

1097 Wijekumar, S., Shahani, U., Simpson, W. a., McCulloch, D.L., 2012b.
1098 Localization of hemodynamic responses to simple visual stimulation: An
1099 fNIRS study. *Investig. Ophthalmol. Vis. Sci.* 53, 2266–2273.
1100 doi:10.1167/iovs.11-8680

1101 Wijekumar, S., Spencer, J.P., Bohache, K.P., Boas, D.A., Magnotta, V.A., 2015.
1102 Validating a new methodology for optical probe design and image
1103 registration in fNIRS studies. *Neuroimage* 106, 86–100.

1104 Xu, Y., Chun, M.M., 2006. Dissociable neural mechanisms supporting visual
1105 short-term memory for objects. *Nature* 440, 91–5. doi:10.1038/nature04262

1106 Yamamoto, T., Kato, T., 2002. Paradoxical correlation between signal in
1107 functional magnetic resonance imaging and deoxygenated haemoglobin
1108 content in capillaries: a new theoretical. *Phys. Med. Biol.* 47, 1121–1141.
1109 doi:10.1088/0031-9155/47/7/309

1110 Yücel, M. a, Selb, J., Cooper, R.J., Boas, D. a, 2014. Targeted Principle
1111 Component Analysis: A new motion artifact correction approach for near-
1112 infrared spectroscopy. *J. Innov. Opt. Health Sci.* 7, 1–8.
1113 doi:10.1142/S1793545813500661

1114 Yücel, M. a., Huppert, T.J., Boas, D. a., Gagnon, L., 2012. Calibrating the BOLD
1115 signal during a motor task using an extended fusion model incorporating
1116 DOT, BOLD and ASL data. *Neuroimage* 61, 1268–1276.
1117 doi:10.1016/j.neuroimage.2012.04.036

1118 Zhang, X., Noah, J.A., Hirsch, J., 2016. Separation of the global and local
1119 components in functional near-infrared spectroscopy signals using principal
1120 component spatial filtering. *Neurophotonics* 3, 015004.
1121 doi:10.1117/1.NPh.3.1.015004
1122

1123 **Supplementary Material**

1124

1125 T1. Number of voxels showing significant positive and negative HbO and HbR correlations with
 1126 BOLD for each of the 12 conditions.

	Number of voxels			
	Positive HbO-BOLD	Positive HbR-BOLD	Negative HbO-BOLD	Negative HbR-BOLD
CR2	360	549	574	516
CR4	389	432	670	309
CR6	494	443	630	438
FA2	490	754	629	69
FA4	483	462	253	248
FA6	239	402	730	336
Hit2	756	782	482	924
Hit4	764	924	294	287
Hit6	304	313	428	551
Miss2	291	436	438	503
Miss4	195	776	370	383
Miss6	343	362	208	263

1127

1128

1129 T2. Regions that showed a positive correlation between BOLD and HbO concentration for Hit4
 1130 trials. Exemplar clusters from tis table have been shown in Figure 7.

Region	Hemi	Peak voxel MNI Coordinates (LPI orientation)			Size (mm ³)	Peak voxel R value
		x	y	z		
Superior parietal lobule	R	28	-80	52	1400	0.9737
Superior parietal lobule	R	18	-86	50	520	0.9752
Inferior parietal lobule	L	-60	-50	36	400	0.8538
Supramarginal gyrus	L	-70	-26	18	1096	0.9955
Postcentral gyrus	R	62	-8	32	312	0.7805
Superior temporal gyrus	R	70	-16	2	280	0.9679
Superior temporal gyrus	R	64	-26	12	520	0.8855
Middle frontal gyrus	R	40	24	48	304	0.7541
Middle frontal gyrus	L	-44	46	20	288	0.8373
Superior frontal gyrus	R	20	60	22	712	0.8696
Cuneus	R	6	-86	42	280	0.7802

1131

1132

1133 T3. Regions that showed a positive correlation between BOLD and HbR concentration for Hit4
 1134 trials.
 1135

Region	Hemi	Peak voxel MNI Coordinates (LPI orientation)			Size (mm ³)	Peak voxel R value
		x	y	z		
Superior parietal lobule	R	18	-86	50	992	0.9821
Superior parietal lobule	R	24	-64	60	352	0.8273
Superior parietal lobule	L	-26	-84	46	272	0.841
Inferior parietal lobule	L	-48	-56	54	256	0.8925
Supramarginal gyrus	L	-70	-26	18	224	0.9523
Superior temporal gyrus	R	58	-20	4	648	0.7788
Middle frontal gyrus	L	-44	44	22	840	0.883
Middle frontal gyrus	R	42	24	48	392	0.7519
Inferior frontal gyrus	R	54	30	22	576	0.8567
Inferior frontal gyrus	L	-40	36	0	544	0.7456
Inferior frontal gyrus	L	-38	10	28	400	0.7788
Inferior frontal gyrus	R	48	38	12	88	0.7159
Superior frontal gyrus	R	22	58	24	752	0.8886
Superior frontal gyrus	R	20	56	10	240	0.7837
Superior frontal gyrus	R	26	58	18	240	0.7852
Superior occipital gyrus	R	20	-78	36	352	0.8394
Cuneus	L	6	-82	42	224	0.7637

1136
 1137
 1138 T4. Regions that showed a positive correlation between BOLD and HbO concentration for CR4
 1139 trials. Exemplar clusters from tis table have been shown in Figure 8.
 1140

Region	Hemi	Peak voxel MNI Coordinates (LPI orientation)			Size (mm ³)	Peak voxel R value
		x	y	z		
Superior parietal lobule	R	18	-86	50	696	0.9719
Superior parietal lobule	R	26	-80	52	632	0.9501
Inferior parietal lobule	L	-50	-50	46	384	0.8477
Postcentral gyrus	R	64	-6	30	632	0.8839
Superior temporal gyrus	L	-60	-34	14	768	0.8242

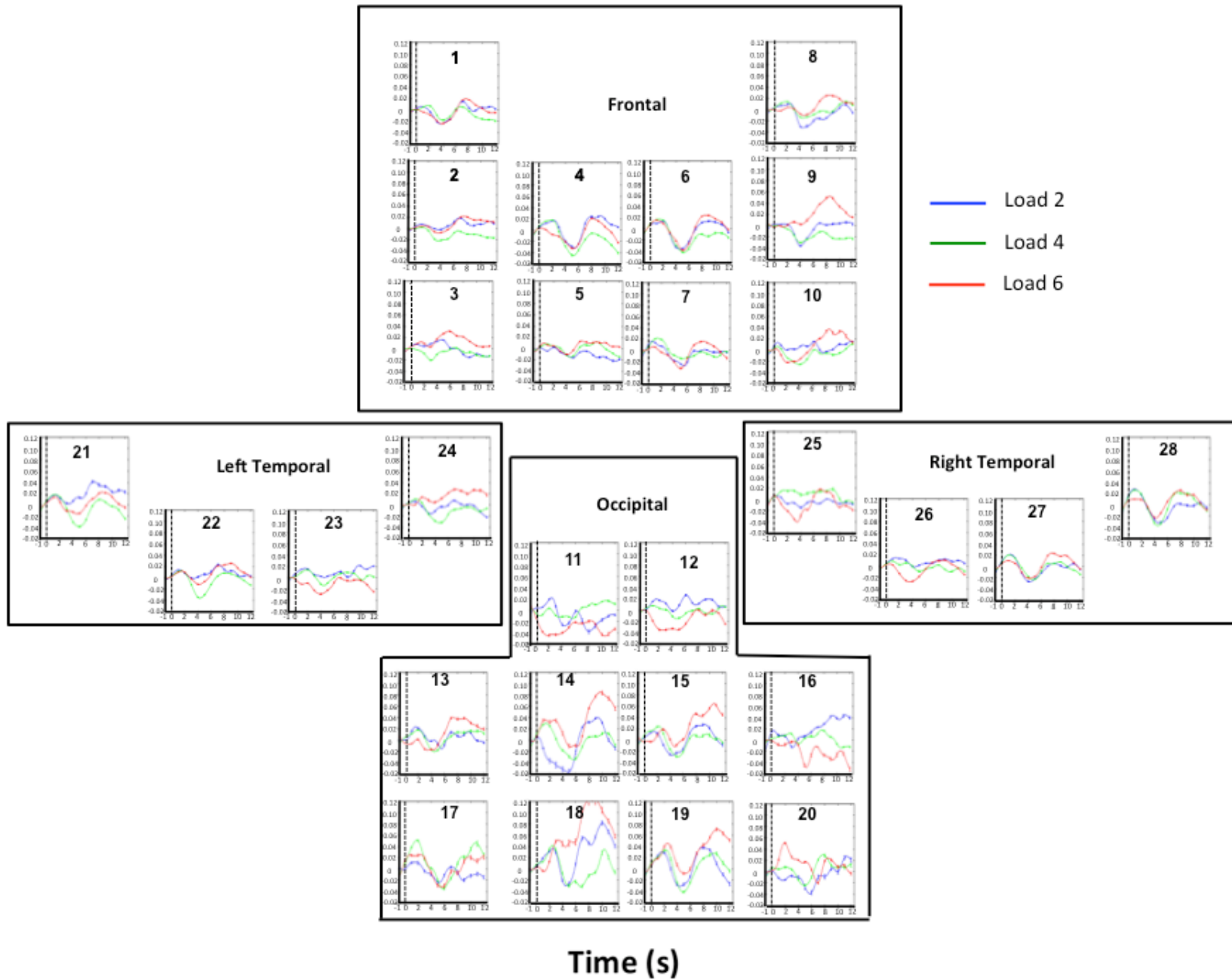
1141
 1142
 1143
 1144
 1145
 1146
 1147

1148 T5. Regions that showed a positive correlation between BOLD and HbR concentration for CR4
 1149 trials.

Region	Hemi	Peak voxel MNI Coordinates (LPI orientation)			Size (mm ³)	Peak voxel R value
		x	y	z		
Inferior parietal lobule	L	-56	-54	42	456	0.8515
Superior parietal lobule	R	18	-86	50	224	0.9633
Postcentral gyrus	R	58	-8	30	24	0.624
Middle frontal gyrus	R	48	42	10	1032	0.8716
Middle frontal gyrus	L	-40	48	20	456	0.8656
Inferior frontal gyrus	R	52	28	20	640	0.9065
Superior frontal gyrus	R	18	58	22	544	0.8267
Cuneus	R	6	-82	44	80	0.7926

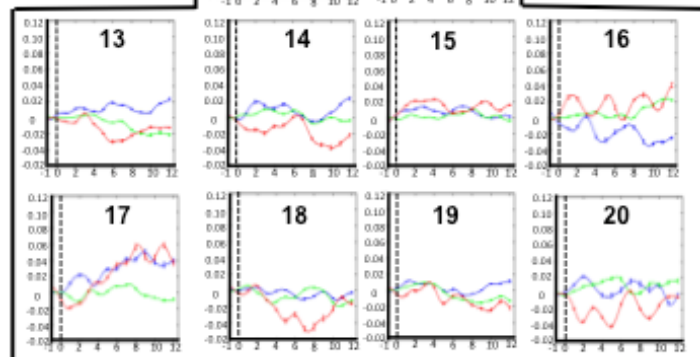
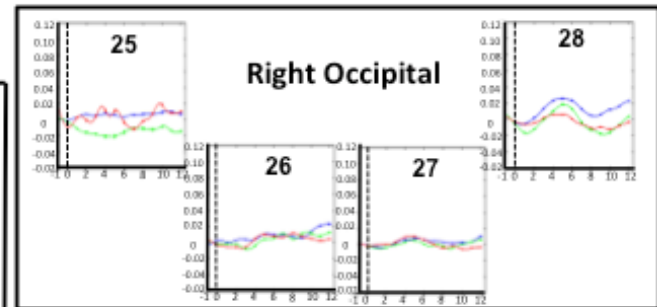
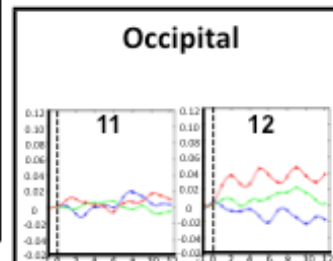
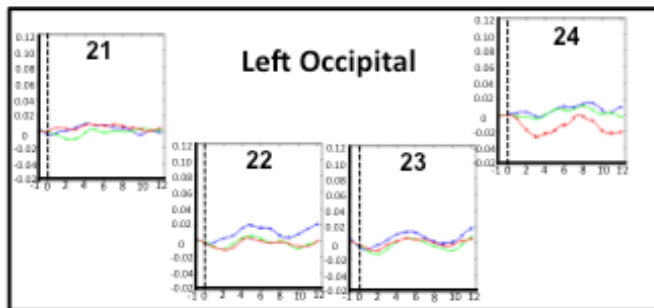
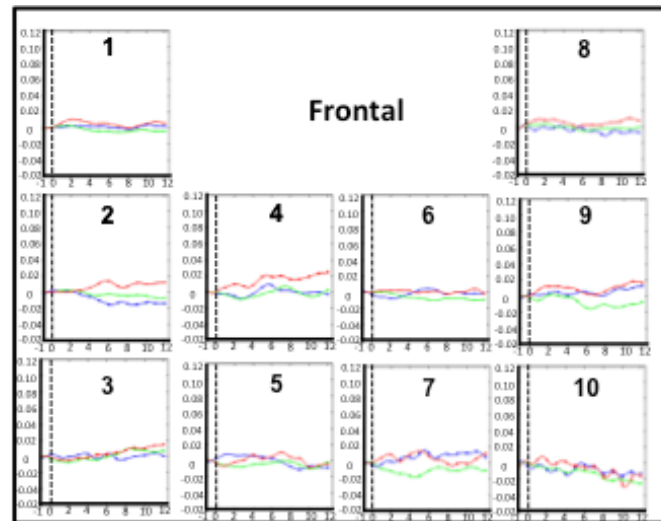
1150
 1151

Change in HbO concentration (μM)



1153 F2. Weighted block average HbO signals for Hit trials for Loads 2 (shown in blue),4 (shown in
1154 green) and 6 (shown in red) across the frontal (outlined in red), temporal (outlined in green) and
1155 parietal (outlines in blue) channels. Figure shown for illustration purposes. Note that GLM
1156 analyses were used for the image-reconstruction approach (see text for details). Dotted line
1157 indicates the onset of the sample array.

Change in HbR concentration (μM)



Time (s)

1159 F3. Weighted block average HbR signals for Hit trials for Loads 2 (shown in blue),4 (shown in
1160 green) and 6 (shown in red) across the frontal (outlined in red), temporal (outlined in green) and
1161 parietal (outlines in blue) channels. Figure shown for illustration purposes. Note that GLM
1162 analyses were used for the image-reconstruction approach (see text for details). Dotted line
1163 indicates the onset of the sample array.

